

## Grazing bifurcations in impact oscillators

Wai Chin,<sup>1,2</sup> Edward Ott,<sup>2,3</sup> Helena E. Nusse,<sup>4,\*</sup> and Celso Grebogi<sup>1,2,4</sup><sup>1</sup>Department of Mathematics, University of Maryland, College Park, Maryland 20742<sup>2</sup>Institute for Plasma Research, University of Maryland, College Park, Maryland 20742<sup>3</sup>Departments of Electrical Engineering and of Physics, and Institute for Systems Research, University of Maryland, College Park, Maryland 20742<sup>4</sup>Institute for Physical Science and Technology, University of Maryland, College Park, Maryland 20742

(Received 13 June 1994)

Impact oscillators demonstrate interesting dynamical features. In particular, new types of bifurcations take place as such systems evolve from a nonimpacting to an impacting state (or vice versa), as a system parameter varies smoothly. These bifurcations are called grazing bifurcations. In this paper we analyze the different types of grazing bifurcations that can occur in a simple sinusoidally forced oscillator system in the presence of friction and a hard wall with which the impacts take place. The general picture we obtain exemplifies universal features that are predicted to occur in a wide variety of impact oscillator systems.

PACS number(s): 05.45.+b

## I. INTRODUCTION

We say that a system is an impact oscillator if it has an oscillating object that impacts frequently with some other object [1,2]. Impact oscillators occur in many technological situations. For example, mechanical devices are often engineered with loose fitting joints to accommodate thermal expansion, and the dynamical behavior of such systems often leads to impacts in the joint. In addition, many machines inevitably suffer from effects of vibroimpacts. A common feature shared by models of these systems is the smoothness of the systems between the impacts. Shaw and Holmes studied a piecewise linear, sinusoidally forced impact oscillator for various values of the forcing frequency [3–6]. Whiston originally showed the importance of *grazing impacts* (i.e., zero velocity impacts) of the global dynamics [7,8]. Recently, Nordmark expanded (to first order) solutions in the neighborhood of a grazing orbit for a simple physical system (described below) and obtained a two dimensional map representing the dynamics of an orbit in the neighborhood of the grazing state [9]. Nordmark also studied the dynamics of this map, obtaining several important results [9,10]; we will give details later. Nusse, Ott, and Yorke [11] obtained results for the dynamics of the one dimensional limit of a two dimensional map equivalent to the map derived by Nordmark. Budd, Dux, and Lamba considered sinusoidally forced impact oscillators, studying such features as chattering, intermittency, the effect of frequency and clearance variations, and the scaling of Lyapunov exponents at nonsmooth bifurcations [12].

In this paper, we use the simple physical system shown in Fig. 1 as a prototype impact oscillator. This is the system considered in [9,10]. A mass  $m$  is attached to a linear spring with spring constant  $k$  that is fixed to the wall on the right hand side. There is a sinusoidal external force  $F_0 \sin \omega t$  acting on the mass. The friction force is proportional to the velocity of the mass with coefficient  $\mu$ . Here  $\xi$  represents the position of the mass  $m$ , and  $\dot{\xi}$  is the time derivative of  $\xi$ , which is the velocity of the mass  $m$ . A hard wall stands at the position  $\xi_c$ . When the amplitude of oscillation is sufficiently small, there are no impacts between the mass  $m$  and the wall at  $\xi_c$ , and the dynamics of the system is the same as that of a forced damped harmonic oscillator without the wall at  $\xi_c$ . As the amplitude of oscillation is increased, the mass  $m$  begins to have impacts with the wall, first with very low velocity. The bordering state between the impacting and nonimpacting is called a *grazing impact*, i.e., when the mass contacts with the wall at  $\xi_c$  with zero velocity. Interesting new bifurcations are observed at grazing, and they are called *grazing bifurcations* [9,10]. (Grazing bifurcations are important physical examples of a general type of bifurcation called “border-collision bifurcations”

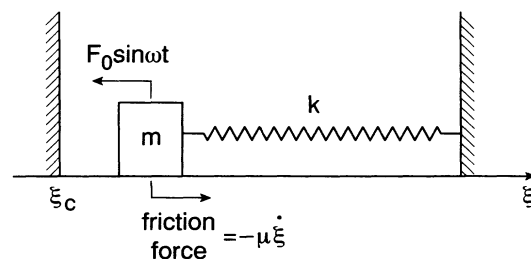


FIG. 1. Our model physical system.

\*Permanent address: Rijksuniversiteit Groningen, Vakgroep Econometrie, Postbus 800, NL-9700 AV Groningen, The Netherlands.

considered in [11,13] and discussed in Sec. VI). The purpose of this paper is to present an analysis of grazing bifurcations for the system in Fig. 1. It is anticipated that these results are universal in that they apply to many systems in which impacts occur.

The two dimensional map derived for the system in Fig. 1 by Nordmark in [9] is equivalent to the following map, which will henceforth be referred to as the Nordmark map:

$$\begin{cases} x_{n+1} = \alpha x_n + y_n + \rho \\ y_{n+1} = -\gamma x_n \end{cases} \text{ for } x_n \leq 0, \quad (1)$$

$$\begin{cases} x_{n+1} = -\sqrt{x_n} + y_n + \rho \\ y_{n+1} = -\gamma \tau^2 x_n \end{cases} \text{ for } x_n > 0. \quad (2)$$

Here  $x_n$  and  $y_n$  are transformed coordinates in the position-velocity space  $(\xi, \dot{\xi})$  evaluated at times  $t_n$ , where  $\omega t_n = 2n\pi$ , and  $\omega$  is the frequency of the external forcing (see Fig. 1). The quantity  $\tau^2$  is the restitution coefficient of the impacts. The relation of  $\gamma$  and  $\alpha$  to the intrinsic properties of the oscillator such as the quantities  $k, m, \omega, \mu$  in Fig. 1 is given in Sec. II. The parameter  $\rho$  is related to  $F_0$ . Equations (1) govern the system if there is no impact between time  $t_n$  and  $t_{n+1}$ . Otherwise, if an impact takes place between  $t_n$  and  $t_{n+1}$ , then Eqs. (2) govern the system. Note that the Nordmark map is continuous at  $x_n = 0$ , but that its Jacobian matrix of partial derivatives is singular at  $x_n = 0$  [in particular,  $\partial x_{n+1} / \partial x_n = -1 / (2\sqrt{x_n})$  for  $x_n > 0$ ]. This singularity at  $x_n = 0$  is responsible for the new bifurcations studied in this paper. The map is normalized so that for fixed  $\gamma$  and  $\alpha$ , the long-time behavior is such that the orbit does not impact with the wall at  $\xi_c$  for  $\rho < 0$ , is in the grazing state for  $\rho = 0$ , and may impact with the wall at  $\xi_c$  for  $\rho > 0$ . Thus if we vary  $\rho$  through zero with fixed  $\gamma$  and  $\alpha$ , the Nordmark map describes the dynamics of an orbit in the neighborhood of the grazing state if  $|\rho| \ll 1$ . Since the map is obtained by expansion of solutions in the neighborhood of the grazing state, its dynamics is related to the physical system only for  $|\rho| \ll 1$ . However, since we are interested in the bifurcations at  $\rho = 0$  (i.e., the grazing bifurcations), the map is expected to capture the universal properties of impact oscillators near grazing. That is, other, physically different systems, when suitably normalized and expanded about the grazing state, should also yield Eqs. (1) and (2).

In what follows we shall be concerned with the bifurcation phenomena for the Nordmark map that occur as the bifurcation parameter  $\rho$  is increased through  $\rho = 0$  (grazing incidence) with  $\gamma$  and  $\alpha$  held fixed. Depending on the values of  $\gamma$  and  $\alpha$  ( $0 < \gamma < 1$ ,  $\alpha < 1 + \gamma$  for physically admissible systems), we observe three basic bifurcation scenarios listed as cases 1–3 below. One of our goals will be to give an analysis to delineate the  $(\gamma, \alpha)$  parameter space into regions in which the bifurcations in each case take place.

*Case 1: Bifurcation from a stable period-1 orbit in  $\rho < 0$  to a reversed infinite period adding cascade as  $\rho$  increases*

*through zero.* Depending on  $\gamma$  and  $\alpha$ , there are two possible forms such a cascade can take: (a) a cascade where chaos appears in bands between successive windows of periodic behavior, and (b) a cascade with hysteresis. Subcase (a) is illustrated by the example shown in Fig. 2(a), while subcase (b) is illustrated by the example shown in Fig. 2(b). (See the figure caption for Figs. 2 for a description of how the bifurcation diagrams are made.) The line in the diagrams occurring for  $\rho < 0$  represents the  $x$  location of an attracting period-1 orbit for the map. Since this period-1 orbit is located in  $x < 0$ , it is determined

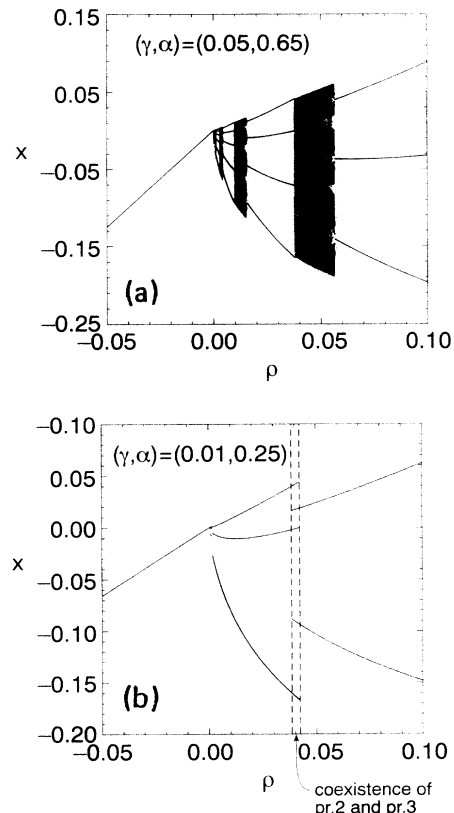


FIG. 2. (a) Bifurcation diagram for  $(\gamma, \alpha) = (0.05, 0.65)$  and  $\tau^2 = 1$ . (b) Bifurcation diagram for  $(\gamma, \alpha) = (0.01, 0.25)$  and  $\tau^2 = 1$ . We use the following steps to produce a bifurcation diagram. (i) Set  $\rho$  to the leftmost value  $\rho_{\min}$  in the figure. [In (a), we start with  $\rho = \rho_{\min} = -0.05$ .] (ii) Set initial point  $(x_0, y_0)$  to an arbitrary point. (iii) Iterate the map 10000 times without plotting anything, to eliminate transient behavior. (iv) Iterate the map another 300 times and plot the resulting 300 values of  $x$ . This is the  $x$  position of the points on the attractor. (v) Increment  $\rho$  by a small amount (in this figure,  $\rho \rightarrow \rho + \frac{1}{4000}$ ), and set the new initial point  $(x_0, y_0)$  to the last point produced in the last step, and return to step (iii). Continue until  $\rho$  reaches the rightmost value  $\rho_{\max}$  in the figure [in (a),  $\rho_{\max} = 0.10$ ]. (vi) If  $\rho_{\max}$  is reached, go to step (v), except now decrease  $\rho$  by a small amount every time (here  $\rho \rightarrow \rho - \frac{1}{4000}$ ) until  $\rho_{\min}$  is reached again. Step (vi) enables us to plot the  $x$  positions of coexisting attractors. The same steps are used to produce Figs. 3–5. The numbers of iterations in steps (iii) and (iv), and the amount of increment in steps (v) and (vi) are varied for each figure.

solely by Eqs. (1). In terms of the system in Fig. 1, this period-1 attractor of the map corresponds to a forced periodic orbit where the mass never impacts the wall. Referring to Fig. 2(a) we see that for subcase (a), as  $\rho$  is decreased from positive values, we encounter windows of stable periodic behavior, and each such window is followed by a band of chaos and then a window of stable periodic behavior whose period is one higher than the period in the previous window. As  $\rho$  decreases, there is an infinite cascade of such windows of ever decreasing width in  $\rho$  and ever increasing period, accumulating on  $\rho=0+$ . To make this phenomenology clearer we plot again in Fig. 3(a) the bifurcation diagram for the same values of  $(\gamma, \alpha)$  as in Fig. 2(a), but now using the variables  $x/\rho$  vs  $\ln \rho$ . We clearly see in this figure that there are six successive period additions with period 3 occurring on the right of the figure and period 9 occurring on the left. Numerically, we find no evidence of any stable periodic orbits other than those in the reversed period adding cascade. Currently we believe that the  $\rho$  intervals between a period  $m$  window and a period  $m+1$  window are occupied entirely by a chaotic attractor. Now refer to Fig. 2(b), which illustrates subcase (b). We see that the  $\rho$  intervals of stable period  $m$  and period  $m+1$  orbits overlap, and chaotic attractors are not present in the cascade.

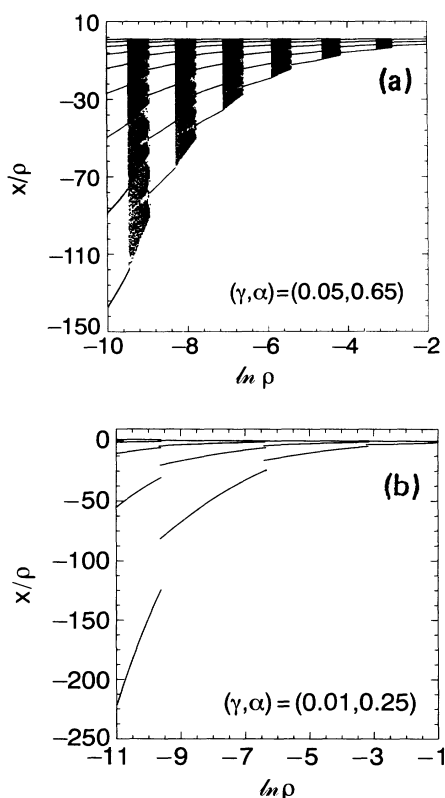


FIG. 3. (a) Bifurcation diagram for  $(\gamma, \alpha) = (0.05, 0.65)$  and  $\tau^2 = 1$  for small positive  $\rho$  values. We plot  $x/\rho$  vs  $\ln \rho$  to take a close look at the dynamics for small positive values of  $\rho$ . (b) Bifurcation diagram for  $(\gamma, \alpha) = (0.01, 0.25)$  and  $\tau^2 = 1$ ,  $x/\rho$  vs  $\ln \rho$ .

Again, this occurs as a reversed infinite period adding cascade. Figure 3(b) is a bifurcation diagram using the variables  $x/\rho$  vs  $\ln \rho$  for the same  $(\gamma, \alpha)$  as for Fig. 2(b). We see three successive period additions in this figure, with period 2 occurring at the right of the figure and period 5 occurring at the left. We have derived a scaling rule for the widths of the periodic windows in terms of  $\gamma$  and  $\alpha$ , applicable to both subcases (a) and (b). The stable periodic orbits in our period adding cascades are numerically observed to be of a very special type. In particular, if the period of the orbit is  $m$ , then the orbit spends one iterate in  $x > 0$  and the other  $m-1$  iterates in  $x < 0$ . We call such a periodic orbit *maximal*. In terms of the system in Fig. 1, a maximal periodic orbit of the map corresponds to a forced periodic orbit where the mass impacts with the wall exactly once per period.

*Case 2: Bifurcation from a stable period-1 orbit in  $\rho < 0$  to a chaotic attractor as  $\rho$  increases through zero.* An example of a bifurcation diagram for this case is shown in Fig. 4(a). We see that as soon as  $\rho$  is increased through zero (corresponding to the occurrence of impacts in Fig. 1), chaos appears. Numerically, we find for Fig. 4(a) that there is no evidence of any window of stable periodic behavior throughout the entire range between  $\rho=0$  and the value of  $\rho$  at which the stable period-2 orbit first ap-

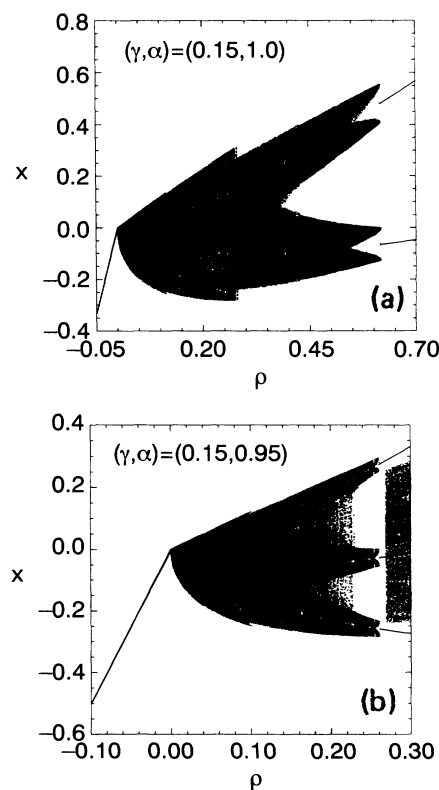


FIG. 4. (a) Bifurcation diagram for  $(\gamma, \alpha) = (0.15, 1.0)$  and  $\tau^2 = 1$ . The highest stable periodic orbit in  $\rho > 0$  has period  $M_0 = 2$ . (b) Bifurcation diagram for  $(\gamma, \alpha) = (0.15, 0.95)$  and  $\tau^2 = 1$ . The highest stable periodic orbit in  $\rho > 0$  has period  $M_0 = 3$ .

pears. In general, case 2 is defined as follows: as  $\rho$  increases from zero there is an interval of  $\rho$  values occupied entirely by a chaotic attractor, and this interval terminates at the appearance of a periodic orbit of some period  $M_0$ . In Fig. 4(a),  $M_0=2$ , but other values of the period  $M_0$  occur depending on the values of  $\gamma$  and  $\alpha$ . Figure 4(b) shows a case where  $M_0=3$ . Indeed, we observed numerically that  $M_0 \rightarrow \infty$  as the boundary in  $(\gamma, \alpha)$  space between case 1 and case 2 is approached from the case 2 side.

*Case 3: Collision of an unstable period- $M$  maximal orbit (which is a regular saddle, and is created, together with a stable period- $M$  maximal orbit, in a saddle-node bifurcation in  $\rho < 0$ ) and the period-1 orbit at  $\rho=0$ .* When plotting a bifurcation diagram, the regular saddle, of course, does not show up. One observes that the attractor is a stable period-1 orbit for  $\rho < 0$  and it is a stable period- $M$  maximal orbit (which is created in the saddle-node bifurcation) for  $\rho > 0$ . Loosely speaking, we will say that there is a (discontinuous) “bifurcation” from a stable period-1 orbit to a stable period- $M$  maximal orbit as  $\rho$  increases through zero. To explain the basic phenomenology of this case, imagine that the orbit is initialized on the period-1 attractor for some negative value of  $\rho$ , and  $\rho$  is then increased very slowly with time. While  $\rho$  remains negative, the orbit tracks the location of the period-1 orbit since the period-1 orbit is attracting for  $\rho < 0$ . However, when  $\rho$  increases through zero, the period-1 orbit becomes unstable and the orbit goes to some other attractor away from the period-1 orbit. We find that this other attractor is always a stable period- $M$  maximal orbit, which is created in a saddle-node bifurcation in  $\rho < 0$ . The unstable period- $M$  maximal orbit created in the same saddle-node bifurcation collides with the period-1 orbit at  $\rho=0$ . Furthermore, we find that at  $\rho=0$ , depending on the parameters  $(\gamma, \alpha)$ , there exists either only one stable maximal periodic orbit or two stable maximal periodic orbits. When two stable maximal periodic orbits coexist, their periods differ by 1. In the cases where two stable maximal orbits coexist, it is always the maximal orbit of lower period that the orbit goes to from the period-1 orbit as  $\rho$  increases slowly from negative to positive values. We call this the “observed” maximal orbit and we say that the period-1 orbit “bifurcates” to this observed maximal periodic orbit as  $\rho$  increases through zero. Figure 5(a) shows a bifurcation diagram for  $(\gamma, \alpha)$  in the region where only a single period-3 stable maximal orbit exists at  $\rho=0$  (this is typical of what happens for other periods). We see that the period-3 stable maximal orbit is born in a saddle-node bifurcation at some negative  $\rho$  value,  $\rho=\rho_3 < 0$ . (The location of the period-3 saddle is indicated by the dashed lines in the figure.) For  $\rho_3 < \rho < 0$ , the stable period-1 orbit coexists with the pair of stable and unstable maximal period-3 orbits created at  $\rho=\rho_3$ . As  $\rho \rightarrow 0^-$ , the unstable period-3 maximal orbit collapses onto the period-1 orbit. The stable period-3 maximal orbit continues to exist in  $\rho > 0$  and the period-1 orbit becomes a flip saddle in  $\rho > 0$ . In addition, we want to point out that the period-3 maximal saddle and the period-1 orbit are involved in the local bifurcation that occurs at  $\rho=0$ , while the stable period-3 maximal orbit is not (since

it is bounded away from the origin). On the other hand, for  $\rho > 0$ , the solutions will converge to the stable period-3 maximal orbit that is created at  $\rho_3$ . Therefore, we call the bifurcation a “bifurcation” from a period-1 attractor to a period-3 attractor. Figure 5(b) shows a bifurcation diagram for  $(\gamma, \alpha)$  in the region where period-3 and period-4 stable maximal orbits coexist at  $\rho=0$ . Now two stable maximal orbits are created in  $\rho < 0$ , the period 3 in a saddle-node bifurcation at  $\rho=\rho_3 < 0$ , and the period 4 in a saddle-node bifurcation at  $\rho=\rho_4 < 0$ , where  $\rho_4 < \rho_3$ . Both stable maximal orbits continue to exist as  $\rho$  becomes positive, but, as already discussed, only the period 3 will be observed to bifurcate from the period-one orbit as  $\rho$  increases through zero. Later on in Sec. V A, it will be explained why this bifurcation to the lower period orbit is observed.

It should be noted that in all three cases above, the stable period-1 orbit that exists in  $\rho < 0$  becomes a *flip saddle* in  $\rho > 0$ . That is, suppose  $\eta$  and  $\kappa$  are eigenvalues

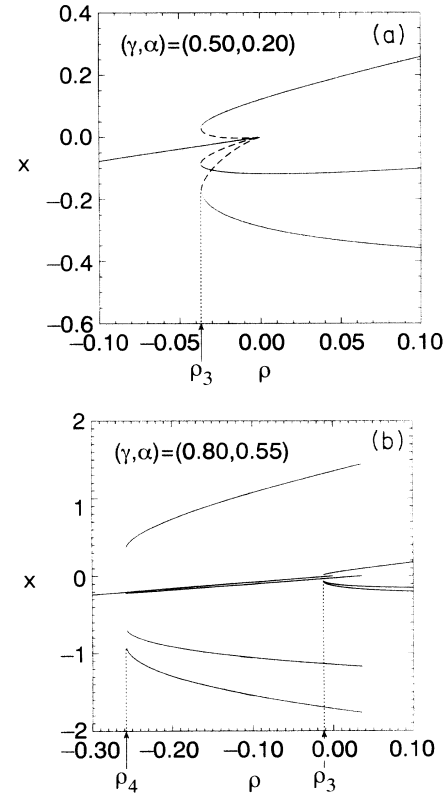


FIG. 5. (a) Bifurcation diagram for  $(\gamma, \alpha) = (0.50, 0.20)$  and  $\tau^2 = 1$ . A stable period-3 maximal orbit and an unstable period-3 maximal orbit are simultaneously created in a saddle-node bifurcation at  $\rho = \rho_3 < 0$ . The dashed curves indicate the locations of the unstable period-3 orbit. The stable period-1 orbit and the stable period-3 orbit are on the solid curves. One can see that the unstable period-3 orbit collapses onto the stable period-1 orbit at  $\rho = 0$ . (b) Bifurcation diagram for  $(\gamma, \alpha) = (0.80, 0.55)$  and  $\tau^2 = 1$ . A pair of stable and unstable period-3 maximal orbits are created in a saddle-node bifurcation at  $\rho = \rho_3 < 0$ , and a pair of stable and unstable period-4 maximal orbits are created in a saddle-node bifurcation at  $\rho = \rho_4 < 0$ . The unstable periodic orbits are not shown.

of the Jacobian matrix at the period-one orbit; then both  $|\eta| < 1$  and  $|\kappa| < 1$  for  $\rho < 0$  and  $\eta < -1 < \kappa < 1$  for  $\rho > 0$ .

The region of  $(\gamma, \alpha)$  space corresponding to systems with non-negative friction [ $\mu \geq 0$  in Fig. 1 and  $\nu \geq 0$  in Eq. (3)] is shown in Fig. 6, where the parameter values corresponding to the various cases in Figs. 2–5 are labeled as points. (The region shown shaded is unphysical and corresponds to negative friction.) As shown subsequently, the requirement of positive friction leads to the restrictions  $0 < \gamma < 1$  and  $\alpha < 1 + \gamma$ . This region is divided into two parts by the parabolic curve  $K$  given by  $\gamma = \alpha^2/4$ . The part above curve  $K$  (i.e., regions I and II) corresponds to overdamping (i.e., the linear harmonic oscillator that results from Fig. 1 with the wall removed is overdamped). This leads to real eigenvalues for the Jacobian matrix of the linear map in Eqs. (1). The part below curve  $K$  (i.e., region III) corresponds to underdamped systems [or systems that have complex conjugate eigenvalues for the Jacobian matrix of the linear map in Eqs. (1)]. Systems with  $(\gamma, \alpha)$  in region I have grazing bifurcations from a period-1 attractor to a reversed infinite period adding cascade (case 1). Systems with  $(\gamma, \alpha)$  in region II experience grazing bifurcations from a period-1 attractor to a chaotic attractor (case 2). Regions I and II are separated by the straight line segment  $\alpha = (\frac{3}{2})\gamma + \frac{2}{3}$  extending downward and leftward from its tangency point with the curve  $K$  at  $(\gamma, \alpha) = (\frac{4}{9}, \frac{4}{3})$  (see Fig. 6). Case 1, subcase (a) [Figs. 2(a) and 3(a)] occurs in the part of region I above the dashed line; case 1, subcase (b) [Figs. 2(b) and 3(b)] occurs in the part of region I below the dashed line. The dashed line segment separating subcases (a) and (b) is given by  $\alpha = 4\gamma + \frac{1}{4}$ , and extends downward and leftward from its point of tangency with the curve  $K$  at  $(\gamma, \alpha) = (\frac{1}{16}, \frac{1}{2})$ . Underdamped systems (region III) have local grazing bifurcation from a period-1 attractor to a period- $M$  attractor (case 3), as in Figs. 5. Recall that the actual bifurcation is a collision of an unstable period- $M$  maximal orbit and the period-1 orbit when  $\rho$  traverses zero. Figure 7(a) shows regions of the  $(\gamma, \alpha)$  space where

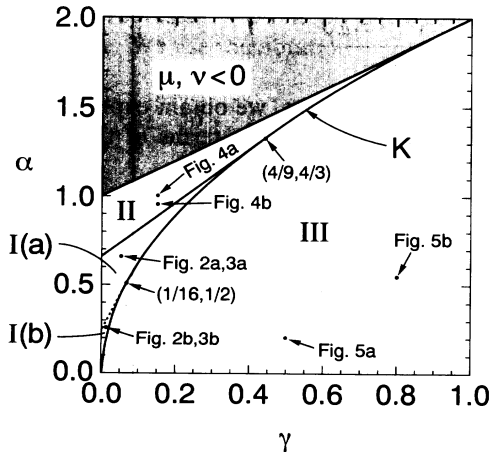


FIG. 6. Regions of the  $(\gamma, \alpha)$  parameter space (unshaded) corresponding to physical systems with positive friction.

stable period- $M$  maximal orbits exist at  $\rho=0$  for  $M=3,4,5,6$  with  $\tau^2=1$ . As already noted, when two such orbits coexist, only the one of lower period will be observed to bifurcate from the period-1 orbit with slowly increasing  $\rho$ . Figure 7(b) [obtained by assigning the overlap regions of the  $(\gamma, \alpha)$  space in Fig. 7(a) to the lower period] shows regions for which the observed bifurcating orbit has period  $M$ . Regions corresponding to higher  $M$  appear in a similar way and accumulate on the curve  $K$  as  $M \rightarrow \infty$ . It will become clear in Secs. IV and V that the delineation of the regions in Fig. 6 is valid for all  $0 \leq \tau^2 \leq 1$ , while the results presented in Figs. 7 is obtained with  $\tau^2=1$ .

Nordmark [9,10] has previously discussed scaling for case 1 and obtained case 2. The existence of the two subcases within case 1, like our treatment of the existence

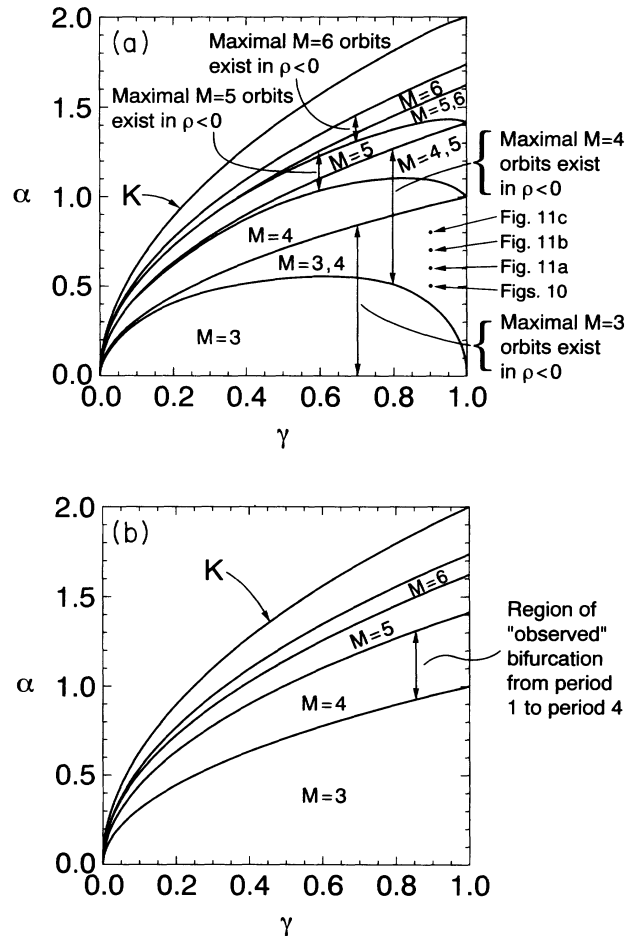


FIG. 7. (a) Regions in the  $(\gamma, \alpha)$  parameter space corresponding to systems in which a stable period- $M$  maximal orbit exists at  $\rho=0$  for  $\tau^2=1$ . Here  $M=3,4,5,6$ . (b) Regions in the  $(\gamma, \alpha)$  parameter space obtained by incorporating the overlap regions in (a) into the regions of the lower period. For systems with  $(\gamma, \alpha)$  in region  $M$ , the stable period-1 orbit is observed to bifurcate to the stable period- $M$  maximal orbit as  $\rho$  increases through zero. The boundary between the regions  $M$  and  $M+1$  is given by  $M\theta = \pi$ .

and stability of maximal orbits for cases 1 and 2 (see Sec. IV), is new. All the results reported for case 3, and the delineation of the  $(\gamma, \alpha)$  parameter space corresponding to each case, are also new.

In Sec. II, explicit relations between  $\gamma$ ,  $\alpha$ , and the physical parameters of the model (Fig. 1) are obtained. Section III derives expressions for maximal periodic orbits. Sections IV and V contain an analysis of the Nordmark map for  $|\rho| \ll 1$ . This includes the existence and stability conditions of maximal periodic orbits for all  $(\gamma, \alpha)$  located in the physically allowed regions in Fig. 6. The analysis results in the division of  $(\gamma, \alpha)$  space into regions corresponding to the different types of grazing bifurcations in the system as explained above, as well as a scaling law for widths of the windows with high periods. Special attention is devoted to the limiting behavior as one approaches the boundaries in Fig. 6. This will, for example, show how an infinite period adding cascade results as one approaches the boundary to region I from one of the other regions. In Sec. VI, we discuss the results of this paper on grazing bifurcations in view of some general results on border-collision bifurcations obtained by Nusse and Yorke in [13]. Conclusions are presented in Sec. VII.

## II. RELATION BETWEEN PHYSICAL QUANTITIES AND PARAMETERS OF THE NORDMARK MAP

In this section we study the relation between the parameters  $\gamma$  and  $\alpha$  and the physical parameters of Fig. 1, namely the mass  $m$ , the spring constant  $k$ , the frequency of the external forcing  $\omega$ , and the friction coefficient  $\mu$ . With these expressions we will be able to understand the physical meaning of results obtained from our analysis of the Nordmark map, which is in terms of  $\gamma$  and  $\alpha$ .

For the physical system in Fig. 1, the equation of motion without impacts with the wall at  $\xi_c$  is

$$\frac{d^2\xi}{d\bar{t}^2} + \nu \frac{d\xi}{d\bar{t}} + \Omega^2 \xi = \bar{F}_0 \sin 2\pi \bar{t}, \quad (3)$$

where we have introduced the quantities  $\nu = 2\pi\mu/m\omega$ ,  $\Omega^2 = 4\pi^2 k/m\omega^2$ , and  $\bar{F}_0 = 4\pi^2 F_0/m\omega^2$ , and normalized time  $t$  so that the external forcing has frequency  $2\pi$  and  $2\pi\bar{t} = \omega t$ . The mapping from  $\bar{t} = n$  to  $\bar{t} = n + 1$  for integer  $n$  is a Poincaré return map on the plane  $(\xi, \dot{\xi})$  with constant phase, and thus has the same set of eigenvalues as the Jacobian matrix of the linear map in Eqs. (1). Let  $P$  be a particular solution of the differential equation (3). Then the general solution of (3) is given by

$$\xi(\bar{t}) = P(\bar{t}) + C_1 e^{s_1 \bar{t}} + C_2 e^{s_2 \bar{t}} \quad \text{if } \nu^2 - 4\Omega^2 \neq 0, \quad (4)$$

and

$$\xi(\bar{t}) = P(\bar{t}) + C_1 e^{s_1 \bar{t}} + C_2 \bar{t} e^{s_1 \bar{t}} \quad \text{if } \nu^2 - 4\Omega^2 = 0,$$

where  $C_1, C_2$  are real numbers and

$$s_1 = \frac{-\nu + \sqrt{\nu^2 - 4\Omega^2}}{2},$$

$$s_2 = \frac{-\nu - \sqrt{\nu^2 - 4\Omega^2}}{2}.$$

From now on, we assume that  $\nu^2 - 4\Omega^2 \neq 0$ . Then we also have the time derivative of  $\xi$  (i.e., velocity of the mass) from Eq. (4):

$$\dot{\xi} = \dot{P} + C_1 s_1 e^{s_1 \bar{t}} + C_2 s_2 e^{s_2 \bar{t}}.$$

Hence for  $\bar{t} = n$ , the state vector in the  $(\xi, \dot{\xi})$  space is

$$\begin{pmatrix} \xi(n) \\ \dot{\xi}(n) \end{pmatrix} = \begin{pmatrix} 1 & 1 \\ s_1 & s_2 \end{pmatrix} \begin{pmatrix} C_1 e^{s_1 n} \\ C_2 e^{s_2 n} \end{pmatrix} + \begin{pmatrix} P \\ \dot{P} \end{pmatrix},$$

and for  $\bar{t} = n + 1$ , we have

$$\begin{aligned} \begin{pmatrix} \xi(n+1) \\ \dot{\xi}(n+1) \end{pmatrix} &= \begin{pmatrix} 1 & 1 \\ s_1 & s_2 \end{pmatrix} \begin{pmatrix} C_1 e^{s_1(n+1)} \\ C_2 e^{s_2(n+1)} \end{pmatrix} + \begin{pmatrix} P \\ \dot{P} \end{pmatrix} \\ &= \mathbf{B} \begin{pmatrix} \xi(n) \\ \dot{\xi}(n) \end{pmatrix} + (\mathbf{1} - \mathbf{B}) \begin{pmatrix} P \\ \dot{P} \end{pmatrix}, \end{aligned}$$

where

$$\mathbf{B} = \begin{pmatrix} e^{s_1} & e^{s_2} \\ s_1 e^{s_1} & s_2 e^{s_2} \end{pmatrix} \begin{pmatrix} 1 & 1 \\ s_1 & s_2 \end{pmatrix}^{-1}. \quad (5)$$

The matrix  $\mathbf{B}$  has the same set of eigenvalues as the Jacobian matrix

$$\mathbf{A} = \begin{pmatrix} \alpha & 1 \\ -\gamma & 0 \end{pmatrix} \quad (6)$$

of the linear map in Eqs. (1). We denote the eigenvalues of matrices  $\mathbf{A}$  and  $\mathbf{B}$  by  $\lambda_1$  and  $\lambda_2$  with  $|\lambda_1| \geq |\lambda_2|$ . From (5) we have

$$\lambda_1 = e^{s_1}, \quad \lambda_2 = e^{s_2}. \quad (7)$$

From (6) we have

$$\lambda_1 = \frac{\alpha + \sqrt{\alpha^2 - 4\gamma}}{2}, \quad (8)$$

$$\lambda_2 = \frac{\alpha - \sqrt{\alpha^2 - 4\gamma}}{2}. \quad (9)$$

Combining these relations, we obtain explicit expressions of the parameters  $\gamma$  and  $\alpha$  in terms of the physical parameters

$$\gamma = \lambda_1 \lambda_2 = e^{s_1 + s_2} = e^{-\nu}, \quad (10)$$

$$\alpha = \lambda_1 + \lambda_2 = e^{s_1} + e^{s_2} = 2e^{-\nu/2} \cosh \left[ \frac{\sqrt{\nu^2 - 4\Omega^2}}{2} \right]. \quad (11)$$

For positive friction  $\nu > 0$ , we have from (10) and (11) that

$$0 < \gamma < 1, \quad 0 < \alpha < 1 + \gamma. \quad (12)$$

This also yields  $|\lambda_1| < 1$  by (8) and (9) and corresponds to

the unshaded region of the  $(\gamma, \alpha)$  space in Fig. 6. Points on the curve  $K$  in Fig. 6 satisfy the relation  $\alpha^2 - 4\gamma = 0$  [or, equivalently,  $\nu^2 - 4\Omega^2 = 0$  by Eqs. (7)–(11)] and correspond to systems with critical damping. Points above the curve  $K$  correspond to overdamped systems (i.e., systems with real eigenvalues  $\lambda_1$  and  $\lambda_2$ ) and points below the curve  $K$  correspond to underdamped systems (i.e., systems with complex conjugate eigenvalues  $\lambda_1$  and  $\lambda_2$ ).

Also notice that  $\gamma$  is related to the friction coefficient by Eq. (10). In the limit of large friction coefficient,  $\nu \rightarrow \infty$ , we have  $\gamma \rightarrow 0$ , and the two dimensional map in Eqs. (1) and (2) reduces to the one dimensional map studied in [11],

$$x_{n+1} = \begin{cases} \alpha x_n + \rho & \text{for } x_n \leq 0, \\ -\sqrt{x_n} + \rho & \text{for } x_n > 0. \end{cases}$$

Case 1 [along with subcases (a) and (b)] and case 2 were found [11] to occur for this one dimensional map for the  $\alpha$  value ranges evident by examining the  $\alpha$  axis (i.e.,  $\gamma = 0$ ) in Fig. 6 [i.e., case 1(a) occurs for  $\frac{1}{4} < \alpha < \frac{2}{3}$ ; case 1(b) occurs for  $0 < \alpha < \frac{1}{4}$ ; and case 2 occurs for  $\frac{2}{3} < \alpha < 1$ ]. In the opposite limit of zero dissipation (i.e.,  $\nu = 0$  and  $\tau^2 = 1$ ), the map given by Eqs. (1) and (2) becomes area preserving. This case has been studied in [12].

### III. MAXIMAL PERIODIC ORBITS

We study the grazing bifurcations at  $\rho = 0$  for Eqs. (1) and (2) in the physically admissible region of the  $(\gamma, \alpha)$  parameter space as characterized in (12). For all these values of  $(\gamma, \alpha)$ , the system has a stable period-1 orbit for small negative  $\rho$  values, which becomes a flip saddle for small positive  $\rho$  values.

Our numerical experiments indicate that only one type of stable periodic orbit is involved in the bifurcations at  $\rho = 0$ . We call such orbits the *maximal* periodic orbits. Here a maximal periodic orbit is a periodic orbit for which exactly one point per period is in the region  $x > 0$ . Our strategy is to find the range of  $\rho$  values in which a period- $m$  maximal orbit exists and the range of  $\rho$  values in which the same orbit is stable.

Let  $(x_n, y_n)$  represent a point on a trajectory of the Nordmark map. We use the notation

$$\phi_n = \begin{bmatrix} x_n \\ y_n \end{bmatrix}, \quad \rho = \begin{bmatrix} \rho \\ 0 \end{bmatrix}, \quad \mathbf{A} = \begin{bmatrix} \alpha & 1 \\ -\gamma & 0 \end{bmatrix}. \quad (13)$$

Then Eqs. (1) can be written as

$$\phi_{n+1} = \mathbf{A}\phi_n + \rho.$$

For a maximal orbit of period  $m$  with trajectory points  $\phi_1, \phi_2, \dots, \phi_m$ , we assume  $x_1 > 0$  so that  $x_2, x_3, \dots, x_m$  are negative and  $\phi_{m+1} = \phi_1$ . Thus

$$\phi_{k+1} = \mathbf{A}^{k-1}\phi_2 + (\mathbf{I} + \mathbf{A} + \mathbf{A}^2 + \dots + \mathbf{A}^{k-2})\rho, \quad (14)$$

where  $k = 2, 3, \dots, m$ . The eigenvalues of  $\mathbf{A}$  are given in Eqs. (8) and (9). Select, for example, the vectors

$$\begin{bmatrix} 1 \\ -\lambda_2 \end{bmatrix}$$

and

$$\begin{bmatrix} 1 \\ -\lambda_1 \end{bmatrix}$$

as eigenvectors corresponding to the eigenvalues  $\lambda_1$  and  $\lambda_2$ , respectively. Write

$$\mathbf{S} = \begin{bmatrix} 1 & 1 \\ -\lambda_2 & -\lambda_1 \end{bmatrix}. \quad (15)$$

Then

$$\mathbf{S}^{-1} = \frac{1}{\lambda_1 - \lambda_2} \begin{bmatrix} \lambda_1 & 1 \\ -\lambda_2 & -1 \end{bmatrix} \quad (16)$$

and

$$\mathbf{A} = \mathbf{S} \begin{bmatrix} \lambda_1 & 0 \\ 0 & \lambda_2 \end{bmatrix} \mathbf{S}^{-1}.$$

Hence, for every integer  $l \geq 0$  we can write

$$\mathbf{I} + \mathbf{A} + \dots + \mathbf{A}^l = \mathbf{S}\Psi^{(l)}\mathbf{S}^{-1},$$

where

$$\Psi^{(l)} = \begin{bmatrix} \psi_1^{(l)} & 0 \\ 0 & \psi_2^{(l)} \end{bmatrix} = \begin{bmatrix} 1 + \lambda_1 + \dots + \lambda_1^l & 0 \\ 0 & 1 + \lambda_2 + \dots + \lambda_2^l \end{bmatrix}. \quad (17)$$

Since by Eqs. (2),

$$\phi_2 = \begin{bmatrix} -\sqrt{x_1 + y_1 + \rho} \\ -\gamma\tau^2 x_1 \end{bmatrix},$$

Eq. (14) can now be written as

$$\begin{aligned} \phi_{k+1} &= \mathbf{S} \begin{bmatrix} \lambda_1^{k-1} & 0 \\ 0 & \lambda_2^{k-1} \end{bmatrix} \mathbf{S}^{-1} \begin{bmatrix} -\sqrt{x_1 + y_1 + \rho} \\ -\gamma\tau^2 x_1 \end{bmatrix} \\ &\quad + \mathbf{S}\Psi^{(k-2)}\mathbf{S}^{-1}\rho \\ &= \mathbf{S} \begin{bmatrix} \lambda_1^{k-1} & 0 \\ 0 & \lambda_2^{k-1} \end{bmatrix} \mathbf{S}^{-1} \begin{bmatrix} -\sqrt{x_1 + y_1} \\ -\gamma\tau^2 x_1 \end{bmatrix} \\ &\quad + \mathbf{S}\Psi^{(k-1)}\mathbf{S}^{-1}\rho, \end{aligned}$$

or

$$\begin{aligned} \mathbf{S}^{-1}\phi_{k+1} &= \begin{bmatrix} \lambda_1^{k-1} & 0 \\ 0 & \lambda_2^{k-1} \end{bmatrix} \mathbf{S}^{-1} \begin{bmatrix} -\sqrt{x_1 + y_1} \\ -\gamma\tau^2 x_1 \end{bmatrix} \\ &\quad + \Psi^{(k-1)}\mathbf{S}^{-1}\rho. \end{aligned} \quad (18)$$

Now let

$$\sigma_k = \mathbf{S}^{-1} \phi_k \equiv \begin{pmatrix} \sigma_k^{(1)} \\ \sigma_k^{(2)} \end{pmatrix},$$

then  $\phi_k = \mathbf{S}\sigma_k$ , and we have

$$\begin{pmatrix} x_k \\ y_k \end{pmatrix} = \begin{pmatrix} \sigma_k^{(1)} + \sigma_k^{(2)} \\ -\lambda_2 \sigma_k^{(1)} - \lambda_1 \sigma_k^{(2)} \end{pmatrix}. \tag{19}$$

Using these notations, we rewrite Eq. (18) as follows:

$$\begin{pmatrix} \sigma_{k+1}^{(1)} \\ \sigma_{k+1}^{(2)} \end{pmatrix} = \begin{pmatrix} \lambda_1^{k-1} & 0 \\ 0 & \lambda_2^{k-1} \end{pmatrix} \mathbf{S}^{-1} \begin{pmatrix} -\sqrt{\sigma_1^{(1)} + \sigma_1^{(2)}} - (\lambda_2 \sigma_1^{(1)} + \lambda_1 \sigma_1^{(2)}) \\ -\gamma \tau^2 (\sigma_1^{(1)} + \sigma_1^{(2)}) \end{pmatrix} + \Psi^{(k-1)} \mathbf{S}^{-1} \rho. \tag{20}$$

This is the mapping from

$$\begin{pmatrix} \sigma_1^{(1)} \\ \sigma_1^{(2)} \end{pmatrix}$$

to

$$\begin{pmatrix} \sigma_{k+1}^{(1)} \\ \sigma_{k+1}^{(2)} \end{pmatrix}$$

for  $k = 1, 2, \dots, m$ , where

$$\begin{pmatrix} \sigma_{k+1}^{(1)} \\ \sigma_{k+1}^{(2)} \end{pmatrix}$$

is related to points on the period- $m$  maximal orbit via Eq. (19).

#### IV. ANALYSIS IN THE CASE OF REAL EIGENVALUES OF EQS. (1)

In this section we assume that  $(\gamma, \alpha)$  lie in the region where the eigenvalues  $\lambda_1$  and  $\lambda_2$  are real (i.e., in the unshaded region above curve  $K$  in Fig. 6).

By dividing both sides of (20) by  $\lambda_1^{2(k-1)}$  and using the notation  $\bar{\Delta}^{(k)} = \Delta / \lambda_1^{2(k-1)}$ , with  $\Delta$  standing for any variable, Eq. (20) takes the form

$$\begin{pmatrix} \bar{\sigma}_{k+1}^{(1)(k)} \\ \bar{\sigma}_{k+1}^{(2)(k)} \end{pmatrix} = \begin{pmatrix} 1 & 0 \\ 0 & \left(\frac{\lambda_2}{\lambda_1}\right)^{k-1} \end{pmatrix} \mathbf{S}^{-1} \begin{pmatrix} -\sqrt{\bar{\sigma}_1^{(1)(k)} + \bar{\sigma}_1^{(2)(k)}} - (\lambda_1)^{k-1} (\lambda_2 \bar{\sigma}_1^{(1)(k)} + \lambda_1 \bar{\sigma}_1^{(2)(k)}) \\ -\gamma \tau^2 (\lambda_1)^{k-1} (\bar{\sigma}_1^{(1)(k)} + \bar{\sigma}_1^{(2)(k)}) \end{pmatrix} + \Psi^{(k-1)} \mathbf{S}^{-1} \bar{\rho}^{(k)}. \tag{21}$$

From Eqs. (8) and (9), we have  $0 < \lambda_2 < \lambda_1 < 1$  for points that are not on the curve  $K$ . Thus  $(\lambda_2/\lambda_1)^k$  and  $(\lambda_1)^k$  both approach zero as  $k$  goes to infinity. Also in the expression of  $\Psi^{(k-1)}$  [cf. Eq. (17)],

$$\psi_i^{(k-1)} = 1 + \lambda_i + \lambda_i^2 + \dots + \lambda_i^{k-1} = \frac{1 - \lambda_i^k}{1 - \lambda_i} \rightarrow \frac{1}{1 - \lambda_i}, \quad k \rightarrow \infty,$$

where  $i = 1, 2$ . Hence for large  $k$  Eq. (21) reduces to

$$\begin{pmatrix} \bar{\sigma}_{k+1}^{(1)(k)} \\ \bar{\sigma}_{k+1}^{(2)(k)} \end{pmatrix} = \begin{pmatrix} 1 & 0 \\ 0 & 0 \end{pmatrix} \mathbf{S}^{-1} \begin{pmatrix} -\sqrt{\bar{\sigma}_1^{(1)(k)} + \bar{\sigma}_1^{(2)(k)}} \\ 0 \end{pmatrix} + \begin{pmatrix} \frac{1}{1 - \lambda_1} & 0 \\ 0 & \frac{1}{1 - \lambda_2} \end{pmatrix} \mathbf{S}^{-1} \bar{\rho}^{(k)} + \mathcal{O}(\max\{\lambda_1^k, (\lambda_2/\lambda_1)^k\}), \tag{22}$$

or, neglecting small terms for  $k \gg 1$ ,

$$\bar{\sigma}_{k+1}^{(1)(k)} = \frac{-\lambda_1}{\lambda_1 - \lambda_2} \sqrt{\bar{\sigma}_1^{(1)(k)} + \bar{\sigma}_1^{(2)(k)}} + \frac{\lambda_1}{(\lambda_1 - \lambda_2)(1 - \lambda_1)} \frac{\rho}{\lambda_1^{2(k-1)}}, \tag{23}$$

$$\bar{\sigma}_{k+1}^{(2)(k)} = \frac{-\lambda_2}{(\lambda_1 - \lambda_2)(1 - \lambda_2)} \frac{\rho}{\lambda_1^{2(k-1)}}. \tag{24}$$

By Eq. (19), Eqs. (23) and (24) give

$$\bar{x}_{k+1}^{(k)} = -\frac{\lambda_1}{\lambda_1 - \lambda_2} \sqrt{\bar{x}_1^{(k)}} + \frac{\bar{\rho}^{(k)}}{1 - \alpha + \gamma}. \tag{25}$$

For the period- $m$  maximal orbit we have  $\bar{x}_{m+1}^{(m)} = \bar{x}_1^{(m)}$ , then Eq. (25) can be solved, yielding (for  $\rho \geq 0$ )

$$\sqrt{\bar{x}_1^{(m)}} = \frac{\lambda_1}{\lambda_1 - \lambda_2} \frac{\sqrt{1 + 4R_m} - 1}{2}, \quad (26)$$

where

$$R_m = \frac{\bar{\rho}^{(m)}}{1 - \alpha + \gamma} \left[ \frac{\lambda_1 - \lambda_2}{\lambda_1} \right]^2.$$

Notice that  $R_m$  and  $\rho$  always have the same signs; see also (12).

Equation (25) also indicates that for large  $m$ , the period- $m$  maximal orbit is stable if

$$\left| \frac{d\bar{x}_{m+1}^{(m)}}{d\bar{x}_1^{(m)}} \right| = \frac{\lambda_1}{\lambda_1 - \lambda_2} \frac{1}{2\sqrt{\bar{x}_1^{(m)}}} < 1. \quad (27)$$

Substituting Eq. (26) for  $\sqrt{\bar{x}_1^{(m)}}$  into (27), we find that the stability condition (27) is equivalent to the inequality

$$\rho > \rho_m^{\text{st}} \approx \frac{3}{4} \left[ \frac{\lambda_1}{\lambda_1 - \lambda_2} \right]^2 (1 - \lambda_1)(1 - \lambda_2)\lambda_1^{2(m-1)}. \quad (28)$$

Meanwhile, multiplying both sides of Eq. (25) by  $\lambda_1^{2(k-1)}$  yields

$$x_{k+1} = -\frac{\lambda_1}{\lambda_1 - \lambda_2} \lambda_1^{k-1} \sqrt{x_1} + \frac{\rho}{1 - \alpha + \gamma},$$

which indicates that  $x_2 < x_3 < \dots < x_m$ . Hence a period- $m$  maximal orbit can exist only if  $x_m < 0$ , or equivalently, by Eqs. (2),  $y_{m+1} = -\gamma\tau^2 x_m > 0$ . By Eq.(19), for large  $m$ , the existence condition for a period- $m$  maximal orbit is

$$\frac{y_{m+1}}{\lambda_1^{2(m-1)}} = -\lambda_2 \bar{\sigma}_{m+1}^{(1)(m)} - \lambda_1 \bar{\sigma}_{m+1}^{(2)(m)} > 0.$$

Using the results from Eqs. (19), (23), (24), and (26) to evaluate the right hand side of the previous equation in terms of  $\lambda_1$ ,  $\lambda_2$ , and  $\rho$ , we find that the existence condition above reduces to

$$\rho < \rho_m^{\text{ex}} \approx \frac{(1 - \lambda_1)^2 (1 - \lambda_2)}{(\lambda_1 - \lambda_2)^2} \lambda_1^{2(m-1)}. \quad (29)$$

The expressions (28) and (29) are key results for our subsequent discussions. We see that a period- $m$  maximal orbit exists for  $\rho < \rho_m^{\text{ex}}$ , and is stable for  $\rho > \rho_m^{\text{st}}$ . Let  $I_m$  denote the interval  $[\rho_m^{\text{st}}, \rho_m^{\text{ex}}]$ . The stable period- $m$  window appears only if the interval  $I_m$  exists, i.e., if  $\rho_m^{\text{ex}} > \rho_m^{\text{st}}$ . From the expressions of  $\rho_m^{\text{st}}$  and  $\rho_m^{\text{ex}}$  in (28) and (29), we see that the interval  $I_m$  shifts to the left (but never reaches zero) for larger values of  $m$ . Thus windows of high period may appear as  $\rho \rightarrow 0+$ . This is in agreement with the phenomena seen in Figs. 2–4.

There are two distinct situations: *case 1* in which  $I_m$  exists for all large  $m$ , and *case 2* in which for every integer  $m > M_0$  (for some threshold  $M_0$ ) the interval  $I_m$  does not exist. The first case implies bifurcations from the period-1 attractor in  $\rho < 0$  to a reversed infinite period

adding cascade in  $\rho > 0$ , and the second case implies bifurcations from the period-1 attractor in  $\rho < 0$  to a chaotic attractor in  $\rho > 0$ . We discuss these two cases separately as follows.

#### A. Case 1: bifurcation from a period-1 attractor to a reversed infinite period adding cascade

The interval  $I_m$  exists for all large  $m$  if  $\rho_m^{\text{ex}} > \rho_m^{\text{st}}$  for all large  $m$ . Then for any period  $m$ , there is an interval  $I_m$  for which the period- $m$  window appears if  $\rho \in I_m$ . Hence there is a reversed infinite cascade of period adding windows as  $\rho \rightarrow 0+$ . Using the expressions of  $\rho_m^{\text{st}}$  and  $\rho_m^{\text{ex}}$  in (28) and (29), we find that  $\rho_m^{\text{ex}} > \rho_m^{\text{st}}$  for all  $m$  sufficiently large if  $\lambda_1 < \frac{2}{3}$ . By Eq. (8) this gives the upper border of region I as shown in Fig. 6, i.e., the straight line segment,

$$\alpha = \frac{3}{2}\gamma + \frac{2}{3}, \quad (30)$$

extending leftward and downward from its point of tangency with the curve  $K$ ,  $(\gamma, \alpha) = (\frac{4}{9}, \frac{4}{3})$ .

Furthermore, from (28) and (29), we can deduce a scaling law for the window widths as  $\rho \rightarrow 0+$ . In particular,

$$\frac{|I_{m+1}|}{|I_m|} = \lambda_1^2, \quad (31)$$

where  $|I_m| = \rho_m^{\text{ex}} - \rho_m^{\text{st}}$  (assuming  $\rho_m^{\text{ex}} > \rho_m^{\text{st}}$  for all large  $m$ ) is the width of the period- $m$  window. This scaling agrees accurately with our numerical results, and it applies (for large  $m$ ) to all systems with  $(\gamma, \alpha)$  in region I in Fig. 6. This scaling law was also obtained in [9].

As indicated in Figs. 2 and 3, there are two different types of reversed cascades of period adding windows. For the first type, the system is chaotic between successive periodic windows in the bifurcation diagram, as in Figs. 2(a) and 3(a). Numerical experiments show no evidence of stable periodic orbits for the  $\rho$  values between the successive maximal periodic windows. For the second type, successive periodic windows overlap, and the system presumably does not have chaotic attractors, as in Figs. 2(b) and 3(b). The first type corresponds to the case in which the neighboring intervals  $I_m$  and  $I_{m+1}$  have no intersection, as schematically shown in Fig. 8(a). The system is presumably chaotic for  $\rho_{m+1}^{\text{ex}} < \rho < \rho_m^{\text{st}}$ . The second type corresponds to the case in which the neighboring intervals  $I_m$  and  $I_{m+1}$  overlap for large  $m$ , as schematically illustrated in Fig. 8(b). The period  $m$  and  $m+1$  orbits coexist for  $\rho_m^{\text{st}} < \rho < \rho_{m+1}^{\text{ex}}$ , and we call this hysteresis. The border between these two types of cascades is  $\rho_m^{\text{st}} = \rho_{m+1}^{\text{ex}}$ , which by (28) and (29) reduces to  $\lambda_1 = \frac{1}{4}$ . By Eq. (8) we find that this border is given by the segment of the line

$$\alpha = 4\gamma + \frac{1}{4}, \quad (32)$$

extending leftward and downward from its point of tangency with the curve  $K$ ,  $(\gamma, \alpha) = (\frac{1}{16}, \frac{1}{2})$ . This is the dashed line in region I in Fig. 6. Systems with  $(\gamma, \alpha)$  falling in the part of region I above the dashed line have  $\rho_{m+1}^{\text{ex}} < \rho_m^{\text{st}}$  for large  $m$ , and the grazing bifurcation at  $\rho = 0$  is from a stable period-1 orbit to a reversed infinite

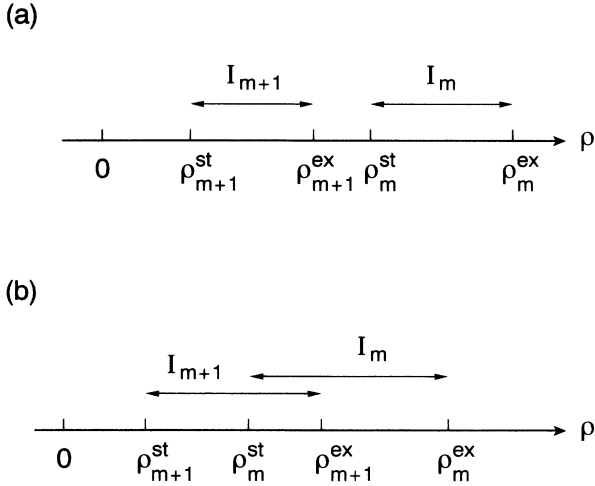


FIG. 8. (a) Schematic illustration of the situation in which intervals  $I_{m+1}$  and  $I_m$  have no intersection. The system is presumably chaotic for  $\rho_{m+1}^{ex} < \rho < \rho_m^{st}$ . (b) Schematic illustration of the situation in which intervals  $I_{m+1}$  and  $I_m$  overlap. Period  $m + 1$  and period  $m$  orbits coexist for  $\rho_m^{st} < \rho < \rho_{m+1}^{ex}$ . This is called hysteresis.

period adding cascade, with chaos between successive windows. Systems with  $(\gamma, \alpha)$  falling in the part of region I below the dashed line have  $\rho_m^{st} < \rho_{m+1}^{ex}$  for large  $m$ , and the experience grazing bifurcations from a stable period-1 orbit to a reversed infinite period adding cascade with hysteresis instead of chaos between successive windows.

**B. Case 2: bifurcation from a period-1 attractor to a chaotic attractor**

Assume there exists a smallest integer  $M_0$  such that  $I_m$  does not exist for  $m > M_0$ . In this case, the reversed period adding phenomenon in the bifurcation diagram stops after period  $M_0$  when the parameter  $\rho$  is decreased. The period of the last window in the bifurcation diagram (which is period  $M_0$ ) is the largest value of  $m$  satisfying  $\rho_m^{ex} > \rho_m^{st}$ . The dynamics is presumably chaotic for all positive  $\rho$  values to the left of that window. Our numerical experiments show no evidence of periodic windows for  $\rho$  values between zero and that window. Thus the bifurcation at  $\rho=0$  is from a stable period-1 orbit to chaos as in Figs. 4. This type of grazing bifurcation from a period-1 attractor to a chaotic attractor occur for systems satisfying  $\rho_m^{ex} < \rho_m^{st}$  for large  $m$ , which, by (28) and (29), reduces to  $\lambda_1 > \frac{2}{3}$ . By Eq. (8) this gives the lower border of region

II as shown in Fig. 6, i.e., the border between regions I and II.

**V. ANALYSIS FOR CASE 3**

The matrix  $A$  has complex conjugate eigenvalues if  $(\gamma, \alpha)$  falls below the curve  $K$  in Fig. 6. Let

$$\lambda_1 = r e^{i\theta} = r (\cos\theta + i \sin\theta),$$

$$\lambda_2 = r e^{-i\theta} = r (\cos\theta - i \sin\theta),$$

where

$$r = \sqrt{\gamma}, \quad \theta = \sin^{-1} \left[ \frac{4\gamma - \alpha^2}{4\gamma} \right]^{1/2}. \tag{33}$$

Note that  $\theta=0$  on the curve  $K$  (given by  $\gamma = \alpha^2/4$ ).

In the region below the curve  $K$  in Fig. 6, we observe grazing bifurcations from a stable period-1 orbit to a stable period- $M$  maximal orbit as  $\rho$  increases through zero (as described in case 3 in Sec. I). Recall that the actual bifurcation is a collision of an unstable period- $M$  maximal orbit and the period-1 orbit. For  $(\gamma, \alpha)$  values below but very close to the curve  $K$ , the grazing bifurcations involve orbits with high periods. In particular,  $M \rightarrow \infty$  as  $\theta \rightarrow 0$  (i.e., as the curve  $K$  is approached from below). When  $\theta$  is not small (i.e., when  $M$  is not large), we concentrate only on the local bifurcation that occurs at  $x=y=0$  as  $\rho \rightarrow 0^-$ ; while for small  $\theta$  (i.e., near the curve  $K$ ) we are able to do more. As  $\rho$  increases from zero, the grazing bifurcation to the period- $M$  maximal orbit is either followed by chaos or by a reversed period adding cascade starting with a period  $M-1$  window. For large  $M$ , we thus also investigate the occurrence and scaling properties of stable maximal periodic orbits in  $\rho > 0$ . This allows us to obtain an understanding of how phenomena below the curve  $K$  match on to those above the curve  $K$  (in particular, how the bifurcation from a stable period-1 orbit to a stable period- $M$  maximal orbit of case 3 goes over to the bifurcation to the reversed infinite period adding cascade of case 1 and the interval of chaos extending from  $\rho=0$  of case 2 as the curve  $K$  is crossed from below.)

**A. When  $\theta$  is not necessarily small**

Our goal in this section is to find the regions under the curve  $K$  in Fig. 6 corresponding to different values of the integer  $M$ . In this case of complex conjugate eigenvalues, we divide both sides of Eq. (20) by  $r^{2(k-1)}$  instead of by  $\lambda_1^{2(k-1)}$ . This time we use the notation  $\bar{\Delta}^{(k)} = \Delta / r^{2(k-1)}$ , where  $\Delta$  stands for any variable. Thus Eq. (20) now takes the form

$$\begin{pmatrix} \bar{\sigma}_{k+1}^{(1)(k)} \\ \bar{\sigma}_{k+1}^{(2)(k)} \end{pmatrix} = \begin{pmatrix} e^{i(k-1)\theta} & 0 \\ 0 & e^{-i(k-1)\theta} \end{pmatrix} \mathbf{S}^{-1} \begin{pmatrix} -\sqrt{\bar{\sigma}_1^{(1)(k)} + \bar{\sigma}_1^{(2)(k)}} - r^{k-1}(\lambda_2 \bar{\sigma}_1^{(1)(k)} + \lambda_1 \bar{\sigma}_1^{(2)(k)}) \\ -r^{k-1} \gamma r^2 (\bar{\sigma}_1^{(1)(k)} + \bar{\sigma}_1^{(2)(k)}) \end{pmatrix} + \Psi^{(k-1)} \mathbf{S}^{-1} \bar{\rho}^{(k)}. \tag{34}$$

Since the integer  $M$  need not be large, we cannot make the approximation  $r^{M-1} \rightarrow 0$ . Thus the terms of order  $r^{k-1}$  may not be dropped, and the quantity  $\psi_1^{(k-1)} = 1 + \lambda_1 + \lambda_1^2 + \dots + \lambda_1^{k-1}$  (where  $i=1,2$ ) in the expression  $\Psi^{(k-1)}$  [cf. Eq. (17)] may not be approximated by  $1/(1-\lambda_i)$ . Then, substituting Eq. (34) into Eq. (19), we find that for a period- $m$  maximal orbit with orbit points  $(x_1, y_1), (x_2, y_2), \dots, (x_m, y_m)$  where  $x_1 > 0$  and  $x_2, x_3, \dots, x_m < 0$ , we have

$$\begin{aligned} \bar{x}_{k+1}^{(k)} &= -\frac{\sin k \theta}{\sin \theta} \sqrt{\bar{x}_1^{(k)}} + \frac{\sin k \theta}{\sin \theta} (\gamma^{(k-1)/2}) \bar{y}_1^{(k)} \\ &\quad - \frac{\sin(k-1)\theta}{\sin \theta} (\gamma^{k/2} \tau^2) \bar{x}_1^{(k)} \\ &\quad + \left[ \frac{\lambda_1 \psi_1^{(k-1)} - \lambda_2 \psi_2^{(k-1)}}{\lambda_1 - \lambda_2} \right] \bar{\rho}^{(k)}, \end{aligned} \quad (35)$$

$$\begin{aligned} \bar{y}_{k+1}^{(k)} &= \frac{\sqrt{\gamma} \sin(k-1)\theta}{\sin \theta} \sqrt{\bar{x}_1^{(k)}} \\ &\quad - \frac{\sin(k-1)\theta}{\sin \theta} (\gamma^{k/2}) \bar{y}_1^{(k)} \\ &\quad + \frac{\sin(k-2)\theta}{\sin \theta} (\gamma^{(k+1)/2} \tau^2) \bar{x}_1^{(k)} \\ &\quad - \left[ \frac{\psi_1^{(k-1)} - \psi_2^{(k-1)}}{\lambda_1 - \lambda_2} \right] \gamma \bar{\rho}^{(k)}, \end{aligned} \quad (36)$$

where again  $k=1,2,\dots,m$ . For the period- $m$  maximal orbit we set  $\bar{x}_1^{(m)} = \bar{x}_{m+1}^{(m)}$  and  $\bar{y}_1^{(m)} = \bar{y}_{m+1}^{(m)}$  in Eqs. (35) and (36); then we have

$$C_x^m \bar{x}_1^{(m)} + \sqrt{\bar{x}_1^{(m)}} + C_\rho^m \bar{\rho}^{(m)} = 0, \quad (37)$$

where

$$\begin{aligned} C_x^m &= \frac{\sin \theta}{\sin m \theta} + \frac{\sin(m-1)\theta}{\sin m \theta} \gamma^{m/2} \tau^2 + \frac{\sin(m-1)\theta}{\sin m \theta} \gamma^{m/2} \\ &\quad + \frac{\sin^2(m-1)\theta}{\sin \theta \sin m \theta} \gamma^m \tau^2 - \frac{\sin(m-2)\theta}{\sin \theta} \gamma^m \tau^2, \end{aligned} \quad (38)$$

$$\begin{aligned} C_\rho^m &= \gamma^{(m+1)/2} \left[ \frac{\psi_1^{(k-1)} - \psi_2^{(k-1)}}{\lambda_1 - \lambda_2} \right] \\ &\quad - \frac{\sin \theta + \gamma^{m/2} \sin(m-1)\theta}{\sin m \theta} \left[ \frac{\lambda_1 \psi_1^{(k-1)} - \lambda_2 \psi_2^{(k-1)}}{\lambda_1 - \lambda_2} \right]. \end{aligned} \quad (39)$$

Regarding (37) as a quadratic equation for  $\sqrt{\bar{x}_1^{(m)}}$ , its two solutions are

$$\sqrt{\bar{x}_{11}^{(m)}} = \frac{-1 + \sqrt{1 - 4C_x^m C_\rho^m \bar{\rho}^{(m)}}}{2C_x^m}, \quad (40)$$

$$\sqrt{\bar{x}_{12}^{(m)}} = \frac{-1 - \sqrt{1 - 4C_x^m C_\rho^m \bar{\rho}^{(m)}}}{2C_x^m}. \quad (41)$$

Notice that the right hand sides of the solutions [Eqs. (40) and (41)] are required to be real and positive.

For the part of  $(\gamma, \alpha)$  parameter space in Fig. 6, numerical computations show that the product  $C_x^m C_\rho^m$  is

nonpositive. With this in mind, we discuss the two kinds of period- $m$  maximal orbits depending on the sign of the quantity  $C_x^m$  as follows:

#### Case (i): $C_x^m < 0$

In this case, both solutions  $\bar{x}_{11}^{(m)}$  and  $\bar{x}_{12}^{(m)}$  can exist. The expressions for  $\sqrt{\bar{x}_{11}^{(m)}}$  and  $\sqrt{\bar{x}_{12}^{(m)}}$  in (40) and (41) indicate that a pair of period- $m$  orbits, corresponding to  $\bar{x}_{11}^{(m)}$  and  $\bar{x}_{12}^{(m)}$ , respectively, are created in a saddle-node bifurcation at some negative  $\rho$  value satisfying

$$1 - 4C_x^m C_\rho^m \bar{\rho}^{(m)} = 0. \quad (42)$$

The orbit corresponding to  $\bar{x}_{11}^{(m)}$  only exists for  $\rho < 0$  [since the right hand side of Eq. (40) is negative for  $\rho > 0$ ] and is numerically observed to always be unstable. In particular, it collapses onto the origin as  $\rho \rightarrow 0^-$ . On the other hand, the orbit corresponding to  $\bar{x}_{12}^{(m)}$  continues to exist up to some positive  $\rho$  value and is observed to remain stable. Figure 5(a) is an example of this scenario. We denote the period of the pair of maximal orbits created in  $\rho < 0$  by  $M$ , and the negative  $\rho$  value satisfying Eq. (42) for  $m=M$  by  $\rho_M$ .

#### Case (ii): $C_x^m > 0$

In this case the orbits corresponding to  $\bar{x}_{11}^{(m)}$  can exist only if  $\rho > 0$  (so that  $\sqrt{\bar{x}_{11}^{(m)}}$  is real and positive) and are observed to be stable only for positive  $\rho$  values bounded away from zero. The solution  $\bar{x}_{12}^{(m)}$  does not exist in this case. Later, in Sec. VB, we consider the periodic orbits in  $\rho > 0$  that correspond to  $\sqrt{\bar{x}_{11}^{(m)}}$  in the limit that the curve  $K$  is approached from below.

From cases (i) and (ii) we see that a pair of stable and unstable period- $M$  maximal orbits are created in  $\rho < 0$  in systems with  $(\gamma, \alpha)$  satisfying  $C_x^M < 0$  and  $\bar{x}_{k+1}^{(M)} < 0$  for  $1 \leq k \leq M-1$  in Eq. (35) for  $\rho=0$ . To delineate the regions of  $(\gamma, \alpha)$  space satisfying these conditions for fixed  $M$  with  $\tau^2=1$ , we take a grid in the region below the curve  $K$  in Fig. 6 and numerically determine from Eqs. (35)–(41) the regions yielding  $C_x^M < 0$  and  $\bar{x}_{k+1}^{(M)} < 0$  for  $1 \leq k \leq M-1$  with  $\rho=0$  and  $\tau^2=1$ . Since all points in the region corresponding to  $M$  are required to yield  $C_x^M < 0$ , and since Eq. (38) indicates that  $C_x^M \rightarrow +\infty$  for  $\sin M \theta \rightarrow 0+$  while  $C_x^M \rightarrow -\infty$  for  $\sin M \theta \rightarrow 0-$ , the upper boundary of the region in the  $(\gamma, \alpha)$  parameter space corresponding to  $M$  is given by

$$M\theta = \pi \quad (43)$$

for all  $0 \leq \tau^2 \leq 1$ . Results for  $M=3,4,5,6$  are shown in Fig. 7(a). (The conditions are never satisfied for  $M=1,2$ .) We find that the regions corresponding to  $M$  and  $M+1$  overlap. For example, in Fig. 7(a) we see that between the regions where only  $M=3$  occurs and only  $M=4$  occurs, there is a region where both  $M=3$  and  $M=4$  occur. For systems with  $(\gamma, \alpha)$  located in the overlap of the regions corresponding to  $M$  and  $M+1$ , a pair of period- $M$  maximal orbits are created in a saddle-node bifurcation at  $\rho = \rho_M < 0$  and a pair of period  $M+1$  maximal orbits are created in a saddle-node bifurcation at

$\rho = \rho_{M+1} < 0$ , where  $\rho_{M+1} < \rho_M$ . Figure 5(b) is an example of this for  $M = 3$ .

Substituting the expression of  $\theta$  in terms of  $\gamma$  and  $\alpha$  given in (33) into Eq. (43), we have

$$\gamma = \frac{\alpha^2}{4[1 - \sin^2(\pi/M)]}. \tag{44}$$

Thus as  $M \rightarrow \infty$ , the regions of successively larger  $M$  accumulate on the curve  $K$  (given by  $\gamma = \alpha^2/4$ ).

For any fixed pair  $(\gamma, \alpha)$  in region III [so  $(\gamma, \alpha)$  is below the curve  $K$ ], we make the following three claims.

*Claim 1.* At most two pairs of maximal orbits, with periods differing by 1, can be created at negative  $\rho$  values. That is, at most two regions, corresponding to  $M$  and  $M + 1$ , respectively, can have overlap.

*Claim 2.* When the parameters  $(\gamma, \alpha)$  are in the region where only one maximal stable periodic orbit is created in  $\rho < 0$ , that orbit is the one that will be *observed* to bifurcate from the stable period-1 orbit as  $\rho$  increases slowly through zero.

To explain what we mean by “observed” in Claim 2, assume that  $\rho$  is initially negative and that the orbit is initially on the period-1 orbit. Now imagine that  $\rho$  is allowed to drift *slowly* upward with time. For  $\rho < 0$  the orbit will track the location of the period-1 orbit because the period-1 orbit is stable. However, when  $\rho$  becomes positive, the period-1 orbit becomes unstable, and the orbit will go to some other attractor. Claim 2 is that the other attractor to which the orbit goes is always the stable maximal periodic orbit.

*Claim 3.* When the parameters  $(\gamma, \alpha)$  are in an overlap region such that maximal stable orbits of period  $M$  and  $M + 1$  are both created in  $\rho < 0$ , the *lower* period stable maximal orbit (i.e., period  $M$ ) is the one that will be *observed* to “bifurcate” from the stable period-1 orbit as  $\rho$  increases slowly through zero.

Thus, Claims 2 and 3 are that the regions of the  $(\gamma, \alpha)$  parameter space corresponding to *observed* bifurcations to a stable period- $M$  maximal orbit are as shown in Fig. 7(b), where Fig. 7(b) is obtained from Fig. 7(a) by incorporating overlap regions into the regions of lower period.

*Derivation supporting Claim 1.* Let  $\phi_1, \phi_2, \dots, \phi_M$  be points on a period- $M$  maximal orbit, assuming  $x_1 > 0$  so that  $x_2, x_3, \dots, x_M < 0$  and  $\phi_{M+1} = \phi_1$ . Then for  $k = 2, 3, \dots, M$  we have  $\phi_{k+1} = \mathbf{A}\phi_k + \rho$  by Eqs. (1), where  $\mathbf{A}$  is defined in Eq. (6). For  $\rho = 0$ ,  $\phi_{k+1} = \mathbf{A}\phi_k$ . We have seen that the matrix  $\mathbf{A}$  can be written as

$$\mathbf{A} = \mathbf{S} \begin{bmatrix} \lambda_1 & 0 \\ 0 & \lambda_2 \end{bmatrix} \mathbf{S}^{-1} = \mathbf{S} \begin{bmatrix} re^{i\theta} & 0 \\ 0 & re^{-i\theta} \end{bmatrix} \mathbf{S}^{-1},$$

where  $\mathbf{S}$  and  $\mathbf{S}^{-1}$  are as in Eqs. (15) and (16). The matrix

$$\begin{bmatrix} e^{i\theta} & 0 \\ 0 & e^{-i\theta} \end{bmatrix}$$

is similar to the rotation matrix

$$\begin{bmatrix} \cos\theta & -\sin\theta \\ \sin\theta & \cos\theta \end{bmatrix}.$$

That is, there exists an invertible matrix  $\mathbf{P}$  such that

$$\begin{bmatrix} e^{i\theta} & 0 \\ 0 & e^{-i\theta} \end{bmatrix} = \mathbf{P} \begin{bmatrix} \cos\theta & -\sin\theta \\ \sin\theta & \cos\theta \end{bmatrix} \mathbf{P}^{-1}.$$

Hence at  $\rho = 0$ ,

$$\phi_{k+1} = \mathbf{A}\phi_k = r\mathbf{S}\mathbf{P} \begin{bmatrix} \cos\theta & -\sin\theta \\ \sin\theta & \cos\theta \end{bmatrix} \mathbf{P}^{-1}\mathbf{S}^{-1}\phi_k.$$

Multiplying both sides by  $\mathbf{P}^{-1}\mathbf{S}^{-1}$ , we have

$$(\mathbf{P}^{-1}\mathbf{S}^{-1}\phi_{k+1}) = r \begin{bmatrix} \cos\theta & -\sin\theta \\ \sin\theta & \cos\theta \end{bmatrix} (\mathbf{P}^{-1}\mathbf{S}^{-1}\phi_k).$$

Thus the points  $\phi_1, \phi_2, \dots, \phi_M$  can be linearly transformed to points  $\phi'_1, \phi'_2, \dots, \phi'_M$  (where  $\phi'_k = \mathbf{P}^{-1}\mathbf{S}^{-1}\phi_k$ ,  $k = 1, 2, \dots, M$ ) that are on a circular arc with an angle  $\theta$  between two successive points (except the one between  $\phi'_1$  and  $\phi'_2$ ), as schematically drawn for  $M = 5$  in Fig. 9. For a maximal periodic orbit the points  $\phi'_2, \phi'_3, \dots, \phi'_M$  are in the left half plane, while the point  $\phi'_1 = \phi'_{M+1}$  is the only point in the right half plane. Write  $\beta_1$  for the angle between the half line through 0 and  $\phi'_2$  and the positive  $y$  axis; and write  $\beta_2$  for the angle between the half line through 0 and  $\phi'_M$  and the negative  $y$  axis (see Fig. 9 for  $M = 5$ ). Now, let  $0 < \beta_1 < \theta$  and  $0 < \beta_2 < \theta$  be given. This implies the following. If  $\beta_1 + \beta_2 \leq \theta$ , then in addition to the stable maximal period- $M$  orbit the Nordmark map may have a stable maximal periodic orbit of period  $M - 1$  but no other stable maximal periodic orbit. Furthermore, if  $\beta_1 + \beta_2 \geq \theta$ , then in addition to the stable maximal period- $M$  orbit the Nordmark map may have a stable maximal periodic orbit of period  $M + 1$  but no other stable maximal periodic orbit. Therefore, the Nordmark map has at most two maximal periodic orbits, with periods differing by 1 and coexisting at  $\rho = 0$ . Hence

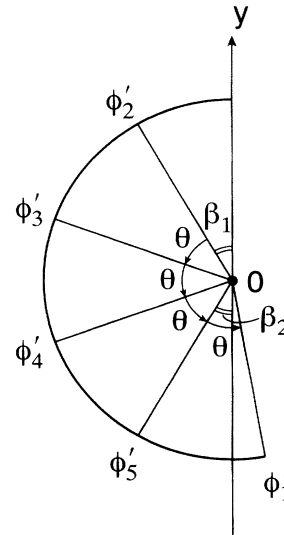


FIG. 9. Schematic positions of (transformed) points on a period-5 maximal orbit.

at most two pairs of maximal orbits can be created at negative  $\rho$  values.

*Support for Claims 2 and 3.* From now on,  $U_0$  denotes a suitable region that includes the origin in its interior. We observed numerically that after its birth at  $\rho_M < 0$ , the stable period- $M$  maximal orbit and its basin of attraction ( $\mathcal{B}_M$ ) are embedded in a region  $U_0$ . This region  $U_0$  was originally occupied by the basin  $\mathcal{B}_1$  of the period-1 orbit. In particular, for  $\rho_M < \rho < 0$ ,  $\mathcal{B}_M$  and  $\mathcal{B}_1$  share the region  $U_0$  that was occupied entirely by  $\mathcal{B}_1$  before the birth of  $\mathcal{B}_M$ . (Here, if two maximal orbits coexist,  $M$  denotes the lower of the two periods.) As  $\rho$  increases toward zero, the area occupied by  $\mathcal{B}_M$  increases and the area occupied by  $\mathcal{B}_1$  diminishes. Roughly speaking, as  $\rho \rightarrow 0^-$  the region that was originally occupied by  $\mathcal{B}_1$  is gradually taken over by  $\mathcal{B}_M$ . In particular,  $\mathcal{B}_1$  shrinks to a finite number of curves emanating from the origin as  $\rho \rightarrow 0^-$ . Meanwhile, the region  $U_0$  occupied by  $\mathcal{B}_M$  and  $\mathcal{B}_1$  combined, as well as the basins of attraction of other stable periodic orbits, are not significantly altered. A region  $U$  that includes  $U_0$  may also have points that belong to basins of stable nonmaximal periodic orbits. As an example illustrating Claim 3, the point  $(\gamma, \alpha) = (0.9, 0.5)$  with  $\tau^2 = 1$  falls in the overlap of regions  $M = 3$  and  $M = 4$  in Fig. 7(a). A pair of period-3 maximal orbits are created in a saddle-node bifurcation at  $\rho = \rho_3$  and a pair of period-4 maximal orbits are created in a saddle-node bifurcation at  $\rho = \rho_4$ , where  $\rho_4 < \rho_3 < 0$ . A stable period-7 orbit (which is not a maximal orbit) also exists. Figures 10 plot basins of different attractors for the system with  $(\gamma, \alpha) = (0.9, 0.5)$  and  $\tau^2 = 1$ : the grey regions are occupied by  $\mathcal{B}_4$  and the black regions are occupied by  $\mathcal{B}_7$ . In Fig. 10(a),  $\rho = -0.02 < \rho_3$ , the period-3 maximal orbits are not yet born, and the white region is occupied by  $\mathcal{B}_1$ . The point marked with a + sign in Fig. 10(a) is the position of the stable period-1 orbit. In Figs. 10(b) and 10(c) [where Fig. 10(c) is an enlargement of the small box in Fig. 10(b)],  $\rho = 0$ , the period-1 orbit has just lost its stability, and the white region is occupied by  $\mathcal{B}_3$ . The three points marked with + signs in Figs. 10(b) and 10(c) are the positions of the stable period-3 maximal orbit. Notice that in Figs. 10(b) and 10(c), the origin (i.e., the position of the period-1 orbit at  $\rho = 0$ ) is embedded in  $\mathcal{B}_3$  and is bounded away from  $\mathcal{B}_7$  and  $\mathcal{B}_4$ . Therefore, if  $\rho$  increases slightly, trajectories that start near the origin will converge to the stable period-3 maximal orbit. This explains why one observes a bifurcation from a fixed point attractor to a period-3 attractor when  $\rho$  traverses zero. This pattern of distribution of  $\mathcal{B}_1$ ,  $\mathcal{B}_M$ , and  $\mathcal{B}_{M+1}$  ( $M = 3$  in Figs. 10) is typical of systems with  $(\gamma, \alpha)$  in the regions where both period  $M$  and period  $M + 1$  maximal orbits are born at negative  $\rho$  values. Therefore only the stable period- $M$  maximal orbit is *observed* to bifurcate from the period-one orbit as  $\rho$  increases through zero for systems with  $(\gamma, \alpha)$  located in the overlap of regions  $M$  and  $M + 1$ .

Figures 11(a)–11(c) are similar plots of basins of attraction as Figs. 10(a)–10(c). (Both Figs. 10 and 11 are produced with the DYNAMICS software [14].) In Figs. 11(a)–11(c),  $\tau^2 = 1$  and  $\rho = 0$  with  $(\gamma, \alpha) = (0.9, 0.6)$  in

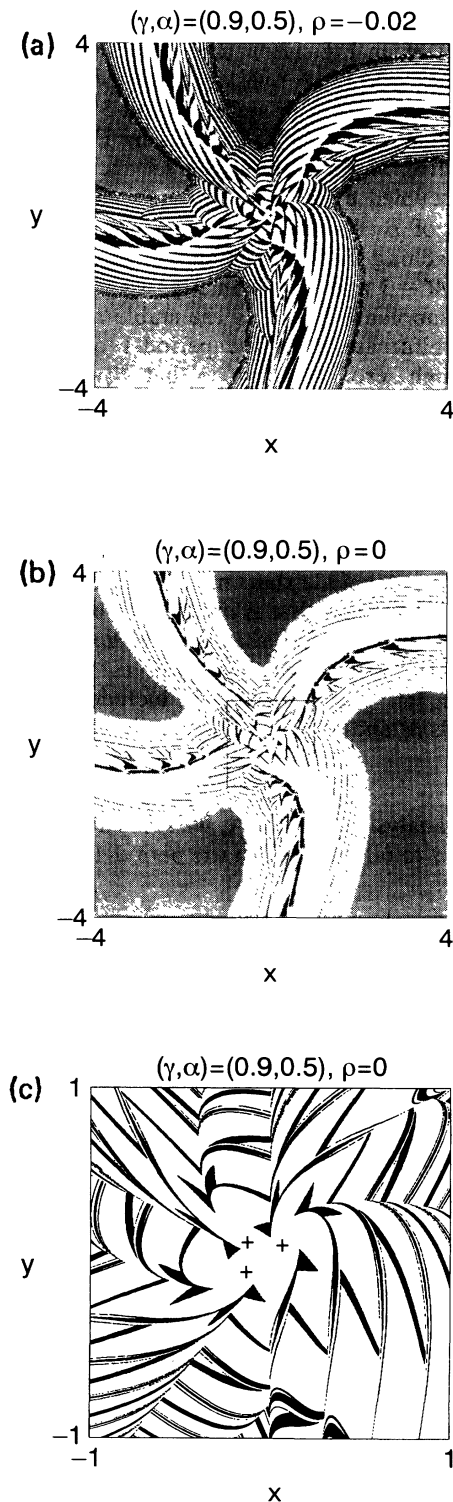


FIG. 10. Basins of attraction for the Nordmark map with  $(\gamma, \alpha) = (0.9, 0.5)$ ,  $\tau^2 = 1$ , and (a)  $\rho = -0.02$ , (b)  $\rho = 0$ , (c)  $\rho = 0$ . Figure 10(c) is an enlargement of the small box in Fig. 10(b). The grey regions in (a)–(c) are occupied by the basin of the stable period-4 maximal orbit; the black regions in (a)–(c) are occupied by the basin of the stable period-7 nonmaximal orbit. The white regions in (a) is the basin of the stable period-1 orbit. The white regions in (b) and (c) are the basin of the stable period-3 maximal orbit.

Fig. 11(a),  $(\gamma, \alpha) = (0.9, 0.7)$  in Fig. 11(b), and  $(\gamma, \alpha) = (0.9, 0.8)$  in Fig. 11(c). The points  $(\gamma, \alpha)$  in Figs. 11(a)–11(c) all fall in the overlap of regions  $M=3$  and  $M=4$  in Fig. 7(a), so both stable period-3 and period-4 maximal orbits exist at  $\rho=0$ . Comparing Fig. 10(b), Fig. 11(a), Fig. 11(b), and Fig. 11(c), we see that at  $\rho=0$  the territories occupied by  $\mathcal{B}_3$  and  $\mathcal{B}_7$  combined are reduced and the area of  $\mathcal{B}_3$  decreases to zero as  $(\gamma, \alpha)$  moves upwards approaching the upper boundary of the overlap of the regions  $M=3$  and  $M=4$  in Fig. 7(a). Thus we see how  $M=4$  supplants  $M=3$  as the stable maximal orbit *observed* to bifurcate from the period-1 orbit as  $\rho$  increases through zero. Also notice that  $\mathcal{B}_7$  no longer exists in Figs. 11(b) and 11(c). [Increasing  $\alpha$  to 1.0 we find that the point  $(\gamma, \alpha) = (0.9, 1.0)$  is in the  $M=4$  region of Fig. 7(a) (i.e., it falls above the overlap of the  $M=3$  and  $M=4$  regions). Then only a pair of period-4 maximal orbits are created in  $\rho < 0$ , and almost every point in the phase space belongs to  $\mathcal{B}_4$  at  $\rho=0$ .]

Therefore we conclude that in the complex eigenvalue case, the maximal orbit that is *observed* to bifurcate from the period-1 orbit as  $\rho$  increases through zero has period  $M$  if  $(\gamma, \alpha)$  falls between the curves  $M\theta = \pi$  and  $(M-1)\theta = \pi$  [cf. Eq. (43)], which includes the region where periods  $M$  and  $M+1$  coexist, as shown in Figs. 7.

### B. Limit of small $\theta$

From the analysis in Sec. V A, we see that the maximal orbit *observed* to bifurcate from the period-1 orbit at  $\rho=0$  has period

$$M = \text{Int} \left[ \frac{\pi}{\theta} \right] + 1, \quad (45)$$

where Int means integer part of. Thus  $M \rightarrow \infty$  as  $\theta \rightarrow 0$  [where  $\theta$  is defined in (33)]. Therefore, in the limit of small  $\theta$ , terms of order  $r^{M-1}$  approach zero and the quantity  $\psi_i^{(M-1)} = 1 + \lambda_i + \lambda_i^2 + \dots + \lambda_i^{M-1}$  (where  $i=1,2$ ) can now be approximated by  $1/(1-\lambda_i)$ . Then Eqs. (35) and (36) in lowest order reduce to

$$\bar{x}_{k+1}^{(k)} = -\frac{\sin k \theta}{\sin \theta} \sqrt{\bar{x}_1^{(k)}} + \frac{\bar{\rho}^{(k)}}{1-\alpha+\gamma}, \quad (46)$$

$$\bar{y}_{k+1}^{(k)} = \sqrt{\gamma} \frac{\sin(k-1)\theta}{\sin \theta} \sqrt{\bar{x}_1^{(k)}} - \frac{\gamma}{1-\alpha+\gamma} \bar{\rho}^{(k)}, \quad (47)$$

where  $k=1,2,\dots,m$ . The expressions of  $C_x^m$  and  $C_\rho^m$  in Eqs. (38) and (39) in lowest order reduce to

$$C_x^m = \frac{\sin \theta}{\sin m \theta}, \quad C_\rho^m = \frac{-\sin \theta}{(1-\alpha+\gamma)\sin m \theta}. \quad (48)$$

Hence the sign of  $C_x^m$  is determined by the sign of  $\sin m \theta$ . The solutions in Eqs. (40) and (41) in lowest order reduce to

$$\sqrt{\bar{x}_{11}^{(m)}} = \frac{-\sin m \theta + \sin m \theta \sqrt{1+4Q_m/\sin^2 m \theta}}{2 \sin \theta}, \quad (49)$$

$$\sqrt{\bar{x}_{12}^{(m)}} = \frac{-\sin m \theta - \sin m \theta \sqrt{1+4Q_m/\sin^2 m \theta}}{2 \sin \theta}, \quad (50)$$

where

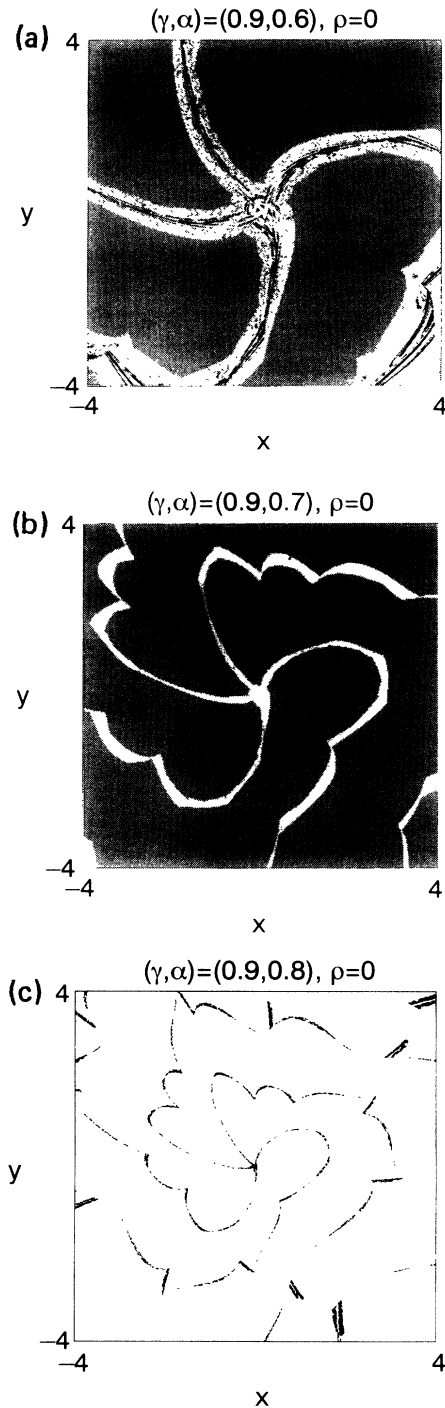


FIG. 11. Basins of attraction for the Nordmark map with  $\tau^2=1$ ,  $\rho=0$ , and (a)  $(\gamma, \alpha) = (0.9, 0.6)$ . The grey region is occupied by the basin of the stable period-4 maximal orbit, the black region by the basin of the stable period-7 nonmaximal orbit, and the white region by the basin of the stable period-3 maximal orbit. (b)  $(\gamma, \alpha) = (0.9, 0.7)$ . The gray region is occupied by the basin of the stable period-4 maximal orbit, and the white region by the basin of the stable period-3 maximal orbit. The stable period-7 nonmaximal orbit no longer exists at this parameter value. (c)  $(\gamma, \alpha) = (0.9, 0.8)$ . For clarity, now the white region is the basin of the stable period-4 maximal orbit, and the black region is the basin of the stable period-3 maximal orbit. The stable period-7 orbit does not exist for this parameter value.

$$Q_m = \frac{\sin^2 \theta}{(1-\alpha+\gamma)} \frac{\rho}{r^{2(m-1)}}.$$

[Notice that  $Q_m$  and  $\rho$  always have the same signs; see also (12).]

Using the approximated expressions above, we reexamine the two kinds of period- $m$  maximal orbits depending on the sign of  $C_x^m$  (as in Sec. V A).

*Case (i):  $C_x^m < 0$*

By Eq. (48), in this case  $\sin m\theta < 0$  and  $m = M$ , where  $M$  is defined in Eq. (45). Then we have from Eqs. (49) and (50) that

$$\sqrt{\bar{x}_{11}^{(M)}} = \frac{-\sin M\theta - \sqrt{\sin^2 M\theta + 4Q_M}}{2 \sin \theta}, \quad (51)$$

$$\sqrt{\bar{x}_{12}^{(M)}} = \frac{-\sin M\theta + \sqrt{\sin^2 M\theta + 4Q_M}}{2 \sin \theta}. \quad (52)$$

According to Eq. (44), regions of successively higher  $M$  in Figs. 7 approach the curve  $K$  (i.e., the parabola  $\gamma = \alpha^2/4$ ). The approximated equation (46) indicates that for large  $M$  only the period- $M$  maximal orbit can exist at  $\rho = 0$ , so that  $\bar{x}_{M+1}^{(M)} > 0$  and  $\bar{x}_{k+1}^{(M)} < 0$  for  $1 \leq k \leq M-1$ . (The phenomenon of the coexistence of two stable maximal orbits of periods  $M$  and  $M+1$  at  $\rho = 0$  is lost due to the approximations made for large  $M$ .)

Moreover, with the approximated expressions (46), (51), and (52), we can easily show that for large  $M$  the maximal period- $M$  orbit corresponding to  $\sqrt{\bar{x}_{11}^{(M)}}$  is always unstable and the maximal period- $M$  orbit corresponding to  $\sqrt{\bar{x}_{12}^{(M)}}$  is always stable (which is observed numerically in Sec. V A). In particular, since  $\sin M\theta < 0$ ,

$$\begin{aligned} \left. \frac{d\bar{x}_{M+1}^{(M)}}{d\bar{x}_1^{(M)}} \right|_{\bar{x}_{11}^{(M)}} &= \frac{-\sin M\theta}{2 \sin \theta \sqrt{\bar{x}_{11}^{(M)}}} \\ &= \frac{-\sin M\theta}{-\sin M\theta - \sqrt{\sin^2 M\theta + 4Q_M}} > 1, \end{aligned}$$

for all negative  $\rho$  values (since  $\bar{x}_{11}^{(M)}$  exists only for  $\rho < 0$ ) satisfying  $\sin^2 M\theta + 4Q_M > 0$ , and

$$\begin{aligned} 0 < \left. \frac{d\bar{x}_{M+1}^{(M)}}{d\bar{x}_1^{(M)}} \right|_{\bar{x}_{12}^{(M)}} &= \frac{-\sin M\theta}{2 \sin \theta \sqrt{\bar{x}_{12}^{(M)}}} \\ &= \frac{-\sin M\theta}{-\sin M\theta + \sqrt{\sin^2 M\theta + 4Q_M}} < 1 \end{aligned}$$

for all  $\rho$  values satisfying  $\sin^2 M\theta + 4Q_M > 0$ .

Notice, however, that for  $\theta \rightarrow 0$ , i.e., when  $(\gamma, \alpha)$  approaches the curve  $K$  from below in Fig. 6, we have  $C_x^M \rightarrow 0$  and  $C_\rho^M \rightarrow 0$ . Then Eq. (37) implies that the period- $M$  maximal orbits shrink to the origin, and thus do not exist.

*Case (ii):  $C_x^m > 0$*

By Eq. (48), in this case  $\sin m\theta > 0$ ; hence  $m < M$ , where  $M$  is defined by Eq. (45). Then we have from Eqs. (49) and (50) that

$$\sqrt{\bar{x}_{11}^{(m)}} = \frac{-\sin m\theta + \sqrt{\sin^2 m\theta + 4Q_m}}{2 \sin \theta}, \quad (53)$$

$$\sqrt{\bar{x}_{12}^{(m)}} = \frac{-\sin m\theta - \sqrt{\sin^2 m\theta + 4Q_m}}{2 \sin \theta}. \quad (54)$$

As discussed in Sec. V A, only the solution  $\sqrt{\bar{x}_{11}^{(m)}}$  is admissible (i.e., real and positive), and the corresponding periodic orbit only exists for positive  $\rho$  values. With the simplified expressions in this section, we are able to explicitly derive the stability and existence conditions for period- $m$  maximal orbits corresponding to  $\sqrt{\bar{x}_{11}^{(m)}}$  for large  $m$  (without creating outrageously messy expressions). Thus we are able to obtain results on the occurrence and scaling properties of the stable maximal orbits with high periods in  $\rho > 0$ .

A maximal orbit with period  $m < M$  is stable if, by Eqs. (46) and (53),

$$\begin{aligned} 0 > \left. \frac{d\bar{x}_{m+1}^{(m)}}{d\bar{x}_1^{(m)}} \right|_{\bar{x}_{11}^{(m)}} &= \frac{-\sin m\theta}{2 \sin \theta \sqrt{\bar{x}_{11}^{(m)}}} \\ &= \frac{-\sin m\theta}{-\sin m\theta + \sqrt{\sin^2 m\theta + 4Q_m}} > -1, \end{aligned}$$

which can be reduced to the inequality

$$\rho > \hat{\rho}_m^{\text{st}} \approx \frac{3}{4}(1-\alpha+\gamma) \frac{\sin^2 m\theta}{\sin^2 \theta} \gamma^{m-1} > 0, \quad (55)$$

where  $\hat{\rho}_m^{\text{st}}$  is the stability threshold in the complex case.

On the other hand, a maximal orbit with period  $m$  can exist if  $x_2, x_3, \dots, x_m < 0$ . Equation (46) indicates that  $x_m = \max\{x_k: 2 \leq k \leq m\}$  for large  $m$ . Hence a maximal orbit with period  $m$  can exist if  $x_m < 0$ , which means that  $y_{m+1} = -\gamma x_m > 0$  by Eqs. (1). Using Eqs. (47) and (53), this reduces to

$$\begin{aligned} \rho < \hat{\rho}_m^{\text{ex}} &\approx \left[ \frac{1-\alpha+\gamma}{\gamma} \frac{\sin^2(m-1)\theta}{\sin^2 \theta} \right. \\ &\quad \left. - \frac{1-\alpha+\gamma}{\sqrt{\gamma}} \frac{\sin(m-1)\theta \sin m\theta}{\sin^2 \theta} \right] \gamma^{m-1}, \end{aligned} \quad (56)$$

where  $\hat{\rho}_m^{\text{ex}}$  is the existence threshold in the complex case.

Thus a stable period- $m$  maximal orbit exists in the  $\rho$  interval  $J_m = [\hat{\rho}_m^{\text{st}}, \hat{\rho}_m^{\text{ex}}]$  if  $\hat{\rho}_m^{\text{ex}} > \hat{\rho}_m^{\text{st}}$ . Using the expressions of  $\hat{\rho}_m^{\text{st}}$  and  $\hat{\rho}_m^{\text{ex}}$  in (55) and (56), the condition  $\hat{\rho}_m^{\text{ex}} > \hat{\rho}_m^{\text{st}}$  yields

$$\gamma < \frac{4}{9} \left[ \frac{\sin(m-1)\theta}{\sin m\theta} \right]^2 \equiv \frac{4}{9} \left[ \cos \theta - \frac{\sin \theta}{\tan m\theta} \right]^2. \quad (57)$$

Notice that for  $\theta \rightarrow 0$ , (57) is satisfied for all large  $m$  if  $\gamma < 4/9$ . Thus for  $\gamma < 4/9$ , as  $\rho$  increases from zero, the grazing bifurcation from the stable period-1 orbit to the stable period- $M$  maximal orbit is followed by a reversed period adding cascade starting with a period  $M-1$  window. The stable periodic orbits in this cascade are the maximal periodic orbits corresponding to  $\bar{x}_{11}^{(m)}$ . Hence, for  $\theta = 0$ , the maximal orbits corresponding to  $\bar{x}_{11}^{(m)}$  form

a reversed infinite period adding cascade in  $\rho > 0$ . This corresponds to points on the curve  $K$  in Fig. 6 with  $\gamma < \frac{4}{9}$ , which is the right hand side border of region I. Moreover, the neighboring intervals  $J_m$  and  $J_{m+1}$  do not overlap if  $\hat{\rho}_{m+1}^{\text{ex}} < \hat{\rho}_m^{\text{st}}$ , which is similar to the schematic illustration in Fig. 8(a), while the intervals  $J_m$  and  $J_{m+1}$  overlap if  $\hat{\rho}_{m+1}^{\text{ex}} > \hat{\rho}_m^{\text{st}}$ , which is similar to the schematic illustration in Fig. 8(b). By the expressions of  $\hat{\rho}_m^{\text{st}}$  and  $\hat{\rho}_m^{\text{ex}}$  in (55) and (56), the condition  $\hat{\rho}_{m+1}^{\text{ex}} > \hat{\rho}_m^{\text{st}}$  yields

$$\gamma < \frac{1}{16} \left[ \frac{\sin m \theta}{\sin(m+1)\theta} \right]^2 \equiv \frac{1}{16} \left[ \cos \theta - \frac{\sin \theta}{\tan(m+1)\theta} \right]^2. \quad (58)$$

For  $\theta \rightarrow 0$ , (58) is satisfied for *all large*  $m$  if  $\gamma < \frac{1}{16}$ . Then there is an integer  $N$  (dependent on  $\gamma$ ) such that all windows of periods  $m > N$  overlap with each other. This corresponds to points on the curve  $K$  in Fig. 6 with  $\gamma < \frac{1}{16}$ , which is the right hand side border of region I(b). Similarly, in the limit of  $\theta \rightarrow 0$ , (57) and the opposite of (58) combined correspond to the right hand side border of region I(a), where the system is chaotic between successive windows with high periods; while the opposite of (57) corresponds to the right hand side border of region II, where the system is chaotic in an interval in  $\rho > 0$  extending from zero (recall that the period- $M$  maximal orbits collapse to the origin as  $\theta \rightarrow 0$ ).

The expressions (55) and (56) also give a scaling (for large  $m$ ) of the window widths  $|J_m| = \hat{\rho}_m^{\text{ex}} - \hat{\rho}_m^{\text{st}}$  in the bifurcation diagram if (57) is satisfied. To simplify the expression, we identify the quantity  $\sin(m-1)\theta$  with  $\sin m \theta$  in (56), and then we have

$$\frac{|J_{m+1}|}{|J_m|} \approx \left[ \frac{\sin(m+1)\theta}{\sin m \theta} \right]^2 \gamma = \left[ \cos \theta + \frac{\sin \theta}{\tan m \theta} \right]^2 \gamma. \quad (59)$$

Since  $\tan m \theta$  decreases towards zero as  $m \theta$  increases towards  $\pi$ , the ratio  $|J_{m+1}|/|J_m|$  grows as  $m$  increases. This scaling for large  $m$  agrees well with numerical experiments. The scaling in Eq. (59) reduces to the scaling in Eq. (31) in Sec. IV as  $\theta \rightarrow 0$ .

Thus we see how the phenomena below the curve  $K$  approach those above  $K$  as  $\theta \rightarrow 0$ .

## VI. DISCUSSION OF THE GRAZING BIFURCATION IN VIEW OF ORBIT INDEX

In the bifurcation theory for maps, attention has been focused on differentiable maps when one or more eigenvalues of a fixed point (or periodic point) cross the unit circle. When this occurs, the nature of the fixed point changes. For example, a fixed point attractor becomes a saddle (possibly a flip saddle) or a repeller. The Nordmark map, however, is *piecewise smooth* and is not differentiable at  $x=0$ . In particular, the Jacobian matrix of the Nordmark map changes discontinuously at  $x=0$  and becomes singular as  $x \rightarrow 0 + [\partial x_{n+1}/\partial x_n = 1/(2\sqrt{x_n})]$ . This singularity is responsible for the new

bifurcation phenomena studied in this paper. According to [13], the fixed point of the Nordmark map, which is an attractor located in  $x < 0$  for  $\rho < 0$  and a flip saddle located in  $x > 0$  for  $\rho > 0$ , is a *border crossing fixed point*; and the grazing bifurcations that take place at  $\rho=0$  are examples of *border-collision bifurcations*. In the rest of this section, we present the precise definitions of the terms used above, introduce the *border-collision bifurcation theorem* obtained by Nusse and Yorke in [13], and discuss the grazing bifurcations analyzed in this paper in the context of the more general results on border-collision bifurcations.

A map is *smooth* if it has a continuous derivative. Here we examine maps that are piecewise smooth, and restrict our attention to those that are smooth in two regions of the plane with the border between these regions being a smooth curve. Let  $\Gamma$  be a smooth curve that divides the plane into two regions denoted by  $R_1$  and  $R_2$ . We say that a map  $F$  from the phase space  $\mathbf{R}^2$  to itself is *piecewise smooth* if (i)  $F$  is continuous and (ii)  $F$  is smooth in both the regions  $R_1$  and  $R_2$ . Let  $F(\cdot, \mu) = F_\mu$  be a one-parameter family of piecewise smooth maps from the phase space  $\mathbf{R}^2$  to itself, which depends smoothly on the parameter  $\mu$ , where  $\mu$  varies in a certain interval on the real line. Let  $E_\mu$  denote a fixed point of  $F_\mu$  defined on  $-\epsilon < \mu < \epsilon$  for some  $\epsilon > 0$ . The position of  $E_\mu$  depends continuously on  $\mu$ . We say  $E_\mu$  is a *border crossing fixed point* if it crosses the border  $\Gamma$  between the two regions  $R_1$  and  $R_2$  as  $\mu$  is varied. Assume that the crossing occurs at  $\mu=0$ . A periodic orbit  $P$  is a border crossing orbit if it includes a point that is a border crossing fixed point under some iterate of the map. If, furthermore, there exists a neighborhood  $U$  of the orbit  $P$  such that  $P$  is the only periodic orbit in  $U$  at  $\mu=0$ , then  $P$  is an *isolated border crossing orbit*.

For a general approach we need the concept of the “orbit index” of a periodic orbit [15]. The orbit index is a number associated with a periodic orbit, and this number is useful in understanding the allowable patterns of bifurcations the orbit undergoes. We say an orbit of period  $p$  is *typical* if its Jacobian matrix (i.e., the Jacobian matrix of the  $p$ th iterate of the map at a point on the orbit) exists and neither  $+1$  or  $-1$  is an eigenvalue (of the Jacobian matrix). For typical orbits, the orbit index is  $-1$ ,  $0$ , or  $+1$ . The orbit index is a bifurcation invariant with respect to, as in our cases, the periodic orbits that collapse onto the fixed point  $E_\mu$  as  $\mu \rightarrow 0$ . That is, the sum of the orbit indices of the periodic orbits that collapse onto the fixed point  $E_\mu$  as  $\mu \rightarrow 0^-$  is equal to the corresponding sum as  $\mu \rightarrow 0^+$ . Suppose a typical periodic orbit  $P$  of a map  $F$  has (minimum) period  $p$ . The orbit index of  $P$  depends on the eigenvalues of the Jacobian matrix  $A_p$  of the map  $F^p$  at one of the points on  $P$ . Let  $m$  be the number of real eigenvalues of  $A_p$  smaller than  $-1$ , and let  $n$  be the number of real eigenvalues of  $A_p$  greater than  $+1$ . The *orbit index*  $I_P$  of  $P$  is defined by

$$\begin{aligned} I_P &= 0 && \text{if } m \text{ is odd,} \\ I_P &= -1 && \text{if } m \text{ is even and } n \text{ is odd,} \\ I_P &= +1 && \text{if both } m \text{ and } n \text{ are even.} \end{aligned}$$

If the orbit index  $= -1$ , then the orbit is a *regular saddle*. If the orbit index  $= 0$ , then the orbit is a *flip saddle*. The typical orbits with orbit index  $+1$  are repellers and attractors and orbits with nonreal eigenvalues. The definition of the orbit index is technical when a point of the orbit lies on the boundary  $\Gamma$  since the Jacobian matrix of the map does not exist for points on the boundary. It is unnecessary to define the orbit index on  $\Gamma$  since we consider orbits for  $\mu \neq 0$ .

For a moment, assume that  $E_\mu$  is in the interior of the region  $R_1$  (or the region  $R_2$ ), and denote  $\eta$  and  $\kappa$  for the eigenvalues of the Jacobian matrix  $DF_\mu(E_\mu)$ . If neither of the two eigenvalues  $\eta$  and  $\kappa$  is on the unit circle, then the fixed point  $E_\mu$  is a *flip saddle* (and has index 0) if  $\eta < -1 < \kappa < 1$ ;  $E_\mu$  is a *regular saddle* (and has index  $-1$ ) if  $-1 < \eta < 1 < \kappa$ ;  $E_\mu$  is a repeller (and has index  $+1$ ) if both  $|\eta| > 1$  and  $|\kappa| > 1$ ; and  $E_\mu$  is an attractor (and has index  $+1$ ) if both  $|\eta| < 1$  and  $|\kappa| < 1$ . (Note that  $E_\mu$  has orbit index  $+1$  if the eigenvalues are not real.) Hence, a typical fixed point is a flip saddle, a regular saddle, a repeller, or an attractor.

Now we introduce the *border-collision bifurcation theorem*. Let the regions  $R_1$  and  $R_2$ , the map  $F_\mu$ , and the fixed point (or periodic point)  $E_\mu$  be as above. Suppose there exists a number  $\epsilon > 0$  such that (i)  $E_0$  is on the border of the two regions  $R_1$  and  $R_2$ , (ii) for  $-\epsilon < \mu < 0$  the fixed point  $E_\mu$  is in the region  $R_1$ , and its index is  $I_1$ , and (iii) for  $0 < \mu < \epsilon$  the fixed point  $E_\mu$  is in the region  $R_2$ , and its index is  $I_2$ . If  $I_1$  and  $I_2$  are different, then (as to be stated next) some bifurcation must occur at  $E_0$  so that the sum of the orbit indices is invariant as  $\mu$  crosses zero. The following "border-collision bifurcation theorem" is obtained in [13]:

*Border-collision bifurcation theorem.* For each two dimensional piecewise smooth map depending smoothly on a parameter  $\mu$ , if the index of an isolated border crossing orbit changes as  $\mu$  crosses zero, then at  $\mu=0$  a bifurcation occurs at this point, a bifurcation involving at least one additional periodic orbit.

This result says that additional fixed points or periodic points must bifurcate from  $E_0$  at  $\mu=0$  if the index of  $E_\mu$  changes as  $\mu$  crosses zero. Since this bifurcation occurs while the fixed point (or periodic point) collides with the border of the regions  $R_1$  and  $R_2$ , we call it a *border-collision bifurcation*. In other words, a border-collision bifurcation is a bifurcation at a fixed point (or periodic point) on the border of the two regions, when the orbit index of the fixed point (or periodic point) before the collision with the border is different from the orbit index of the fixed point (or periodic point) after the collision.

Therefore, if the orbit index of a fixed point (or periodic orbit) is different before and after it crosses the border  $\Gamma$ , the following two things can possibly occur.

- (i) There are additional periodic orbits which collapse onto  $E_0$  as  $\mu \rightarrow 0+$  and/or  $\mu \rightarrow 0-$ , whose individual indices are such as to make the total orbit index conserved.
- (ii) One or more chaotic sets collapse onto  $E_0$  as

$\mu \rightarrow 0+$  and/or  $\mu \rightarrow 0-$ . (Since the orbit index for a chaotic set is not defined, conservation of the index is no longer an issue.)

The border separating the two regions in which the Nordmark map is smooth is the line  $x=0$ . The fixed point in the Nordmark map crosses the border  $x=0$  at  $\rho=0$ ; thus it is a border crossing fixed point. For  $\rho < 0$ , the fixed point is in the region  $x < 0$  and is stable (thus it has orbit index  $I_1 = +1$ ); for  $\rho > 0$ , the fixed point is in the region  $x > 0$  and is a flip saddle (thus it has orbit index  $I_2 = 0$ ). We find numerically that it is an isolated saddle at  $\rho=0$ . Since  $I_1 \neq I_2$ , by the *border-collision bifurcation theorem*, there must be other orbits (periodic or chaotic) that collapse onto the fixed point at  $\rho=0$  and are involved in the bifurcation there.

For systems with  $(\gamma, \alpha)$  in the region I (Case 1) in Fig. 6, a reversed infinite period adding cascade collapses onto the fixed point [located at  $(0,0)$ ] as  $\rho \rightarrow 0+$ . Conservation of the orbit index before and after the bifurcation at  $\rho=0$  is not violated in this case, because the orbit index of the stable periodic orbits in the infinite cascade is  $+1$  and the orbit index of the chaotic sets in the infinite cascade is not defined. For systems with  $(\gamma, \alpha)$  in the region II (Case 2) in Fig. 6, a chaotic set collapses onto the fixed point as  $\rho \rightarrow 0+$ , whose orbit index is not defined. As for systems with  $(\gamma, \alpha)$  in the region III (Case 3), which is below the curve  $K$  in Fig. 6, an unstable period- $M$  maximal orbit (which is a regular saddle and thus has orbit index  $-1$ ) collapses onto the fixed point as  $\rho \rightarrow 0-$ . The value of  $M$  is determined by Eq. (45). Therefore the sum of the orbit indices is invariant (and equals zero) as the fixed point crosses the border  $x=0$ . Hence the grazing bifurcations studied in this paper are border-collision bifurcations involving different types of orbits that collapse onto the fixed point as  $\rho \rightarrow 0+$  or  $\rho \rightarrow 0-$ .

## VIII. CONCLUSION

We have observed three major types of grazing bifurcations: (i) bifurcations from a stable period-1 orbit to a reversed infinite period adding cascade; (ii) bifurcation from a stable period-1 orbit to attracting chaos occupying a full interval of the bifurcation parameter; and (iii) collision of an unstable maximal periodic orbit and a period-1 orbit, which is *observed* to be a local bifurcation from a stable period-1 orbit to a stable maximal periodic orbit. These bifurcations are "unconventional" in that they do not occur in smooth systems. Since the Nordmark map represents the dynamics of typical systems that have low-velocity impacts and that are smooth between the impacts, the bifurcations studied in this paper are expected to be universal for such systems.

## ACKNOWLEDGMENTS

This work was supported by the Department of Energy (Office of Scientific Computing, Office of Basic Energy Sciences) and by the Office of Naval Research (Physics).

- [1] F. C. Moon, *Chaotic vibrations* (Wiley, New York, 1987).
- [2] J. M. T. Thompson and R. Ghaffari, *Phys. Rev. A* **27**, 1741 (1983).
- [3] S. W. Shaw and P. J. Holmes, *J. Sound Vib.* **90**, 129 (1983).
- [4] S. W. Shaw and P. J. Holmes, *J. Appl. Mech.* **50**, 849 (1983).
- [5] S. W. Shaw and P. J. Holmes, *Phys. Rev. Lett.* **51**, 623 (1983).
- [6] S. W. Shaw, *J. Sound Vib.* **99**, 199 (1985).
- [7] G. S. Whiston, *J. Sound Vib.* **118**, 395 (1987).
- [8] G. S. Whiston, *J. Sound Vib.* **152**, 427 (1992).
- [9] A. B. Nordmark, *J. Sound Vib.* **145**, 279 (1991).
- [10] A. B. Nordmark, *J. Bifur. Chaos* **2**, 597 (1992).
- [11] H. E. Nusse, E. Ott, and J. A. Yorke, *Phys. Rev. E* **49**, 1073 (1994).
- [12] C. Budd and F. Dux, *Philos. Trans. R. Soc. London A* **347**, 365 (1994); C. Budd and F. Dux, *Nonlinearity* **7**, 1191 (1994); H. Lamba (unpublished); H. Lamba and C. Budd, *Phys. Rev. E* **50**, 84 (1994).
- [13] H. E. Nusse and J. A. Yorke, *Physica D* **57**, 39 (1992).
- [14] H. E. Nusse and J. A. Yorke, *Dynamics: Numerical Explorations* (Springer-Verlag, New York, 1994).
- [15] J. Mallet-Paret and J. A. Yorke, *J. Diff. Equ.* **43**, 419 (1982).

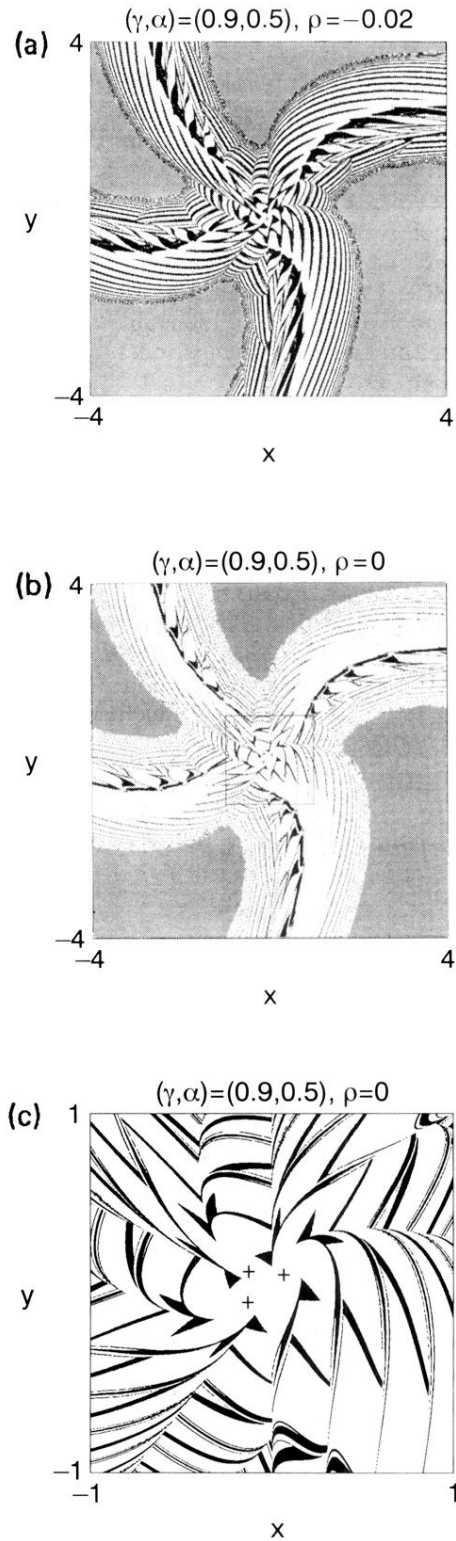


FIG. 10. Basins of attraction for the Nordmark map with  $(\gamma, \alpha) = (0.9, 0.5)$ ,  $\tau^2 = 1$ , and (a)  $\rho = -0.02$ , (b)  $\rho = 0$ , (c)  $\rho = 0$ . Figure 10(c) is an enlargement of the small box in Fig. 10(b). The grey regions in (a)–(c) are occupied by the basin of the stable period-4 maximal orbit; the black regions in (a)–(c) are occupied by the basin of the stable period-7 nonmaximal orbit. The white regions in (a) is the basin of the stable period-1 orbit. The white regions in (b) and (c) are the basin of the stable period-3 maximal orbit.

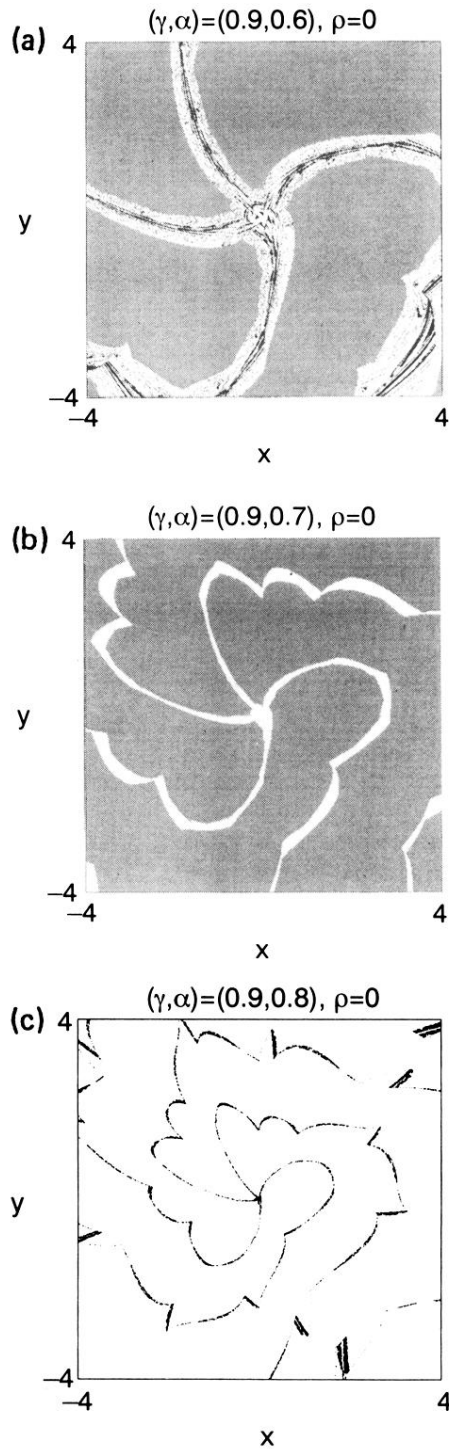


FIG. 11. Basins of attraction for the Nordmark map with  $\tau^2 = 1, \rho = 0$ , and (a)  $(\gamma, \alpha) = (0.9, 0.6)$ . The grey region is occupied by the basin of the stable period-4 maximal orbit, the black region by the basin of the stable period-7 nonmaximal orbit, and the white region by the basin of the stable period-3 maximal orbit. (b)  $(\gamma, \alpha) = (0.9, 0.7)$ . The gray region is occupied by the basin of the stable period-4 maximal orbit, and the white region by the basin of the stable period-3 maximal orbit. The stable period-7 nonmaximal orbit no longer exists at this parameter value. (c)  $(\gamma, \alpha) = (0.9, 0.8)$ . For clarity, now the white region is the basin of the stable period-4 maximal orbit, and the black region is the basin of the stable period-3 maximal orbit. The stable period-7 orbit does not exist for this parameter value.

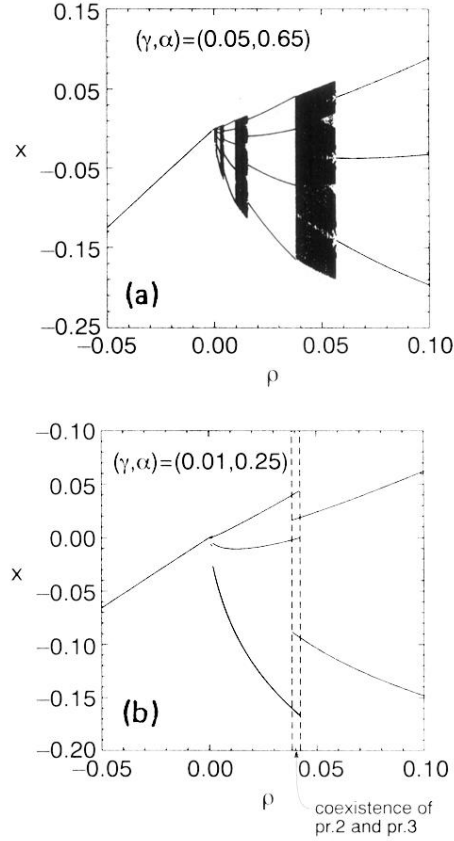


FIG. 2. (a) Bifurcation diagram for  $(\gamma, \alpha) = (0.05, 0.65)$  and  $\tau^2 = 1$ . (b) Bifurcation diagram for  $(\gamma, \alpha) = (0.01, 0.25)$  and  $\tau^2 = 1$ . We use the following steps to produce a bifurcation diagram. (i) Set  $\rho$  to the leftmost value  $\rho_{\min}$  in the figure. [In (a), we start with  $\rho = \rho_{\min} = -0.05$ .] (ii) Set initial point  $(x_0, y_0)$  to an arbitrary point. (iii) Iterate the map 10 000 times without plotting anything, to eliminate transient behavior. (iv) Iterate the map another 300 times and plot the resulting 300 values of  $x$ . This is the  $x$  position of the points on the attractor. (v) Increment  $\rho$  by a small amount (in this figure,  $\rho \rightarrow \rho + \frac{1}{4000}$ ), and set the new initial point  $(x_0, y_0)$  to the last point produced in the last step, and return to step (iii). Continue until  $\rho$  reaches the rightmost value  $\rho_{\max}$  in the figure [in (a),  $\rho_{\max} = 0.10$ ]. (vi) If  $\rho_{\max}$  is reached, go to step (v), except now *decrease*  $\rho$  by a small amount every time (here  $\rho \rightarrow \rho - \frac{1}{4000}$ ) until  $\rho_{\min}$  is reached again. Step (vi) enables us to plot the  $x$  positions of coexisting attractors. The same steps are used to produce Figs. 3–5. The numbers of iterations in steps (iii) and (iv), and the amount of increment in steps (v) and (vi) are varied for each figure.

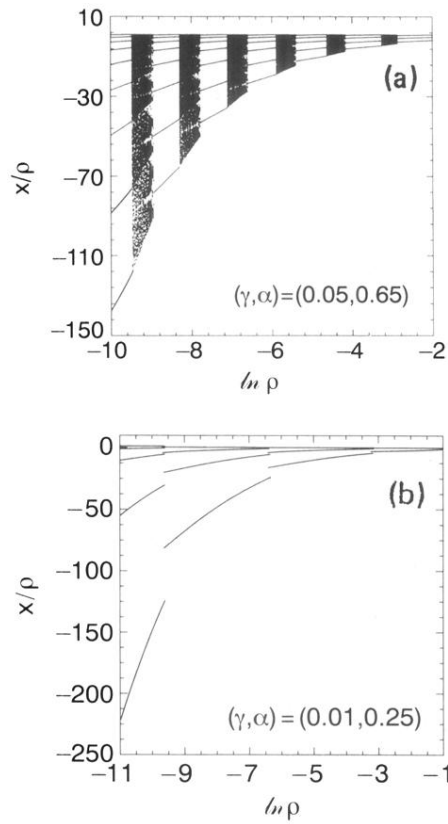


FIG. 3. (a) Bifurcation diagram for  $(\gamma, \alpha) = (0.05, 0.65)$  and  $\tau^2 = 1$  for small positive  $\rho$  values. We plot  $x/\rho$  vs  $\ln \rho$  to take a close look at the dynamics for small positive values of  $\rho$ . (b) Bifurcation diagram for  $(\gamma, \alpha) = (0.01, 0.25)$  and  $\tau^2 = 1$ ,  $x/\rho$  vs  $\ln \rho$ .

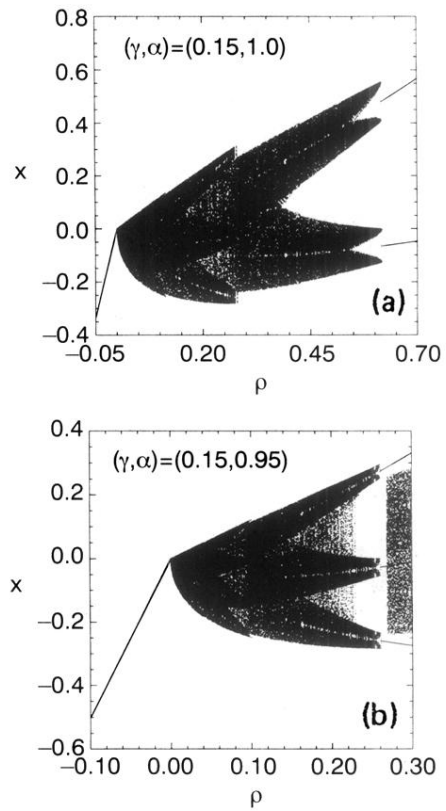


FIG. 4. (a) Bifurcation diagram for  $(\gamma, \alpha) = (0.15, 1.0)$  and  $\tau^2 = 1$ . The highest stable periodic orbit in  $\rho > 0$  has period  $M_0 = 2$ . (b) Bifurcation diagram for  $(\gamma, \alpha) = (0.15, 0.95)$  and  $\tau^2 = 1$ . The highest stable periodic orbit in  $\rho > 0$  has period  $M_0 = 3$ .

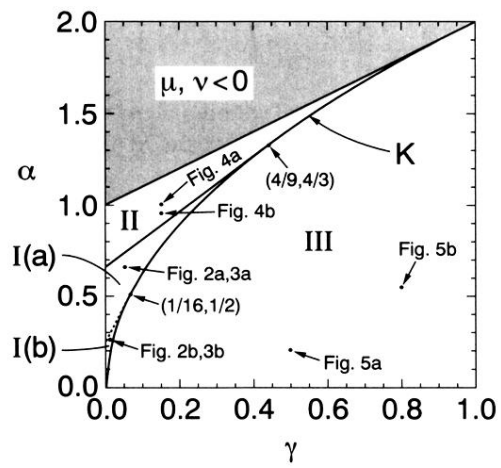


FIG. 6. Regions of the  $(\gamma, \alpha)$  parameter space (unshaded) corresponding to physical systems with positive friction.